Journal Pre-proof

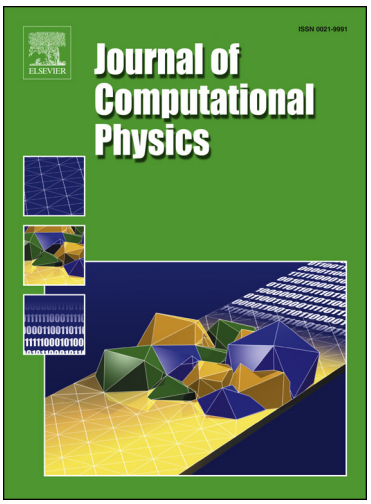

Towards sodium combustion modelling with liquid water

Damien Furfaro, Richard Saurel, Lucas David, François Beauchamp

PII: S0021-9991(19)30765-X
DOI: https://doi.org/10.1016/j.jcp.2019.109060
Reference: YJCPH 109060

To appear in: *Journal of Computational Physics*

Received date: 26 March 2019
Revised date: 16 September 2019
Accepted date: 19 October 2019

Please cite this article as: D. Furfaro et al., Towards sodium combustion modelling with liquid water, *J. Comput. Phys.* (2019), 109060, doi: https://doi.org/10.1016/j.jcp.2019.109060.

Highlights

- A diffuse interface model with enhanced physics and thermochemistry is built for the computation of sodium combustion with liquid water.
- HLLC-type Riemann solvers with both gravity and surface tension are built.
- The thermo-chemical Leidenfrost-type effect responsible for autonomous drop motion in accordance with experimental observations is qualitatively reproduced.
- Explosion effect with shock wave emission and sodium ejection is reproduced as well.

Towards sodium combustion modelling with liquid water

Damien Furfaro [(1)], Richard Saurel [(1,2)], Lucas David [(2,3)] and François Beauchamp [(3)]

[(1)] RS2N SAS, Saint Zacharie, France
[(2)] Aix Marseille Univ, CNRS, Centrale Marseille, LMA, Marseille, France
[(3)] CEA Cadarache, LTRS, Saint-Paul-lez-Durance, France

Abstract

Solid and liquid sodium combustion with liquid water occurs through a thin gas layer where exothermic reactions happen with sodium and water vapors. It thus involves multiple interfaces separating liquid and gas in the presence of surface tension, phase transition, heat and mass diffusion as well as surface reactions. The gas phase reaction involves compressible effects resulting in possible shock wave appearance in both gas and liquid phases. To understand and predict the complexity of sodium combustion with water a diffuse interface flow model is built. This formulation enables flow resolution in multidimension in the presence of complex motion, such as for example Leidenfrost-type thermo-chemical flow. More precisely sodium drop autonomous motion on the liquid surface is computed. Various modelling and numerical issues are present and addressed in the present contribution. Explosion phenomenon is addressed in this paper and is reproduced at least qualitatively thanks to additional ingredients such as turbulent mixing of sodium and water vapors in the gas film and delayed ignition modeled through finite rate chemistry. Shock wave emission from the thermo-chemical Leidenfrost-type flow is observed as well as liquid sodium ejection off the water surface, as reported in related experiments.

emails:
damien.furfaro@rs2n.eu
richard.saurel@univ-amu.fr
lucas.david@cea.fr
francois.beauchamp@cea.fr

1. Introduction

Sodium Fast Reactors (SFR) as well as other engineering systems use sodium (N_a) as coolant fluid. Sodium presents excellent physical properties regarding heat transfer efficiency as well as ability to maintain kinetic energy of fast neutrons. However, it reacts exothermically with both air and water. In the limit, explosion may occur resulting in shock wave propagation in the liquid and surrounding media.

When a liquid or solid sodium drop is set on a liquid water surface surprising phenomenon occurs. A reaction appears rapidly resulting in autonomous drop motion on the liquid surface. It seems that the drop is separated from liquid water by a small gas layer where combustion occurs both in the gas phase and at sodium surface. The phenomenon is reminiscent of the Leidenfrost effect except that the heat used to vaporize sodium and water comes from the combustion of themselves and their vapors. This combustion induces liquid water evaporation and heating of the sodium drop. After some delay, typically a few seconds, explosion occurs. These complex events are qualitatively reported on many videos available on the web, such as [www.youtube.com/watch?v=ODf_sPexS2Q] for example. They clearly illustrate complexity of the physics and chemistry in presence.

Quantitative analytic experiments have been carried out at CEA Cadarache, France, in the facilities SOCRATE, DINAMO, VIPERE and LAVINO (Carnevali 2012, Carnevali et al. 2013, Daudin 2015, Daudin et al. 2018, David et al. 2019). These experiments confirm an important fact: liquid sodium and liquid water are always separated by a gas layer or bubbly zone, resulting in significant lowering of the energy release efficiency compared to the theoretical one. To be more precise, typical reactions of sodium with water assume (ideal) molecular mixing, resulting in energy release of the order of 100 kJ/mol, which is considerable. However, in the experiments and engineering situations of interest, sodium is never mixed with water at molecular scale. Materials are separated by interfaces and the gas layer repels the reactive material (Na) from the oxidizer (water). It results in low energy release rate, with mechanical consequences and blast effects much lower than if the reaction was occurring with molecularly mixed materials. In the limit, reactive materials never mix because of projections, resulting in incomplete reaction, with moderate energy release.

The present work attempts to model these effects to understand and predict the physics occurring in this complex two-phase combustion system. To determine the effective energy release and its kinetics in situations relevant to SFR safety, the mixing process between combustible sodium and oxidizer (water) must be modelled. Mixing of reactants controls the energy release rate. This mixing seems to occur through the gas layer separating the two liquids, resulting in temperature and pressure rise through exothermic reactions occurring in the gas phase and at the sodium surface, resulting in turn to autonomous drop motion and possibly explosion.

Among the former contributions, Marfaing (2014) and Marfaing et al. (2014) considered both liquid and vapor water in the presence of a diffusion flame in 1D spherical configuration. The assumption of 1D flow seemed restrictive, as in reality gas escapes from the film to the atmosphere, as illustrated in the Figure 1.

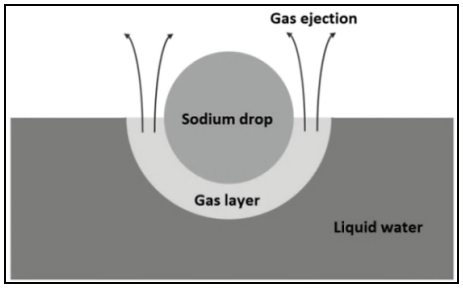

Figure 1: Schematic representation of a floating sodium drop at the surface of liquid water separated by a gas layer. The gas layer thickness is controlled by gas ejection, density difference between the liquids, diffusion fluxes in the gas layer, phase change at interfaces and exothermicity of the reactions, at sodium surface and in the gas mixture.

In this context, gas layer thickness determination is very important as it controls heat and mass diffusion fluxes between sodium and water, responsible for reactants gas mixing and chemical

reaction. As illustrated in Figure 1, self-selection of the gas layer thickness is directly linked to multidimensional effects. A 1D approach can difficulty tackle this problem and has another restriction, such as liquid caustic soda layer appearance, resulting in extra separation of reactants. It seems that the main motivation of 1D computations relied in simplicity to compute material interfaces as they can be explicitly tracked. Marfaing et al. (2014) used an Arbitrary Lagrangian Eulerian (ALE) formulation in this aim.

Multidimensional (multi-D) modelling has been addressed in some contributions dealing with water and sodium interaction. For example, Deguchi et al. (2015) considered interaction of water vapor flow with a liquid sodium interface at rest through a diffusion flame. Another effort is done with the SERAPHIM code (Uchibori et al., 2012) where multi-D computations of sodium drops in water vapor is addressed. However, the approaches considered seem very different to the one promoted in the present contribution. In SERAPHIM averaged two-phase flow equations with two velocities are used to address water vapor interaction with a cloud of sodium droplets. The physics of this interaction is not explicitly addressed but modeled through various correlations. In the present work a single velocity formulation is used to address DNS-type computations to precisely understand and reproduce the physics of this interaction.

Specifically, the present approach is based on diffuse interface formulation, such as described for example in Saurel and Pantano (2018) review. In this context, interface deformations are captured routinely, as shocks and contact surfaces are captured in conventional gas dynamics computations. Moreover, diffuse interface approaches seem able to address the underlying physics and chemistry present in the sodium-water reaction. Indeed, the relevant phenomena to address are:

- Fluids compressibility and the possible presence of shock waves;
- Presence of interfaces with complex physics, such as compressible effects, surface tension, phase transition, chemical species and thermal diffusions as well as surface reactions;
- Intense motion, the interfaces being mobile and deformable;
- Chemical reactions in the gas phase.

As thermal diffusion is present, as argued in Le Martelot et al. (2014) and Saurel et al. (2016) a single temperature diffuse interface model is relevant. Such two-phase model is reminiscent of the reactive Euler equations widely used in combustion, but with thermodynamic closure significantly different from the Dalton's law (Chiapolino et al., 2017a). From this basic flow model, extra physics is included, such as the various chemical reactions and multiple phase transitions as liquid water, sodium and soda evaporate. It seems that a diffuse interface approach was considered as well by Aksenova et al. (2017) and Chudanov et al. (2019) in the same aim as in the present work but with reduced physics.

Diffuse interfaces methods also have limitations, the most restrictive one being the excessive numerical diffusion of material interfaces for long time evolutions. Thanks to the sharpening method of Chiapolino et al. (2017b), based on a specific gradient limiter embedded in the MUSCL scheme (Van Leer, 1979), interfaces are captured with almost 2-3 mesh points at any time, improving significantly capabilities of these methods. Another difficulty is related to the treatment of thermal and molecular diffusion with numerically diffuse interfaces. This issue is addressed in the present paper. Another one is related to the correct numerical treatment of capillary forces and curvature computation, that are challenging when interfaces are sharpened. This issue is addressed as well.

The present paper is organized as follows. The multi-D multiphase flow model in velocity, pressure and temperature equilibrium, complemented with various physicochemical effects is presented in Section 2. The thermodynamic closure is given in Section 3. The numerical method used to solve the overall model is detailed in Section 4. In Section 5, effects of the various physical ingredients (phase transition, heat and mass diffusion, surface and volume chemical reactions) are illustrated in 1D spherical tests. 2D results are presented in Section 6 showing efficient computations of thermochemical Leidenfrost-type effect. Besides, multidimensional explosions with shock wave emission are computed, as reported in related experiments. Liquid sodium ejection from the water surface is also reproduced numerically.

2. Multiphase model and properties

With diffuse interface approaches, the entire domain is considered as a multiphase mixture and interfaces correspond to zones where mixture density, mass and volume fractions are discontinuous. The model considered hereafter is an extension of the one of Le Martelot et al. (2014) and Saurel et al. (2016) developed to model phase change at interfaces. Relevant literature in this frame may be found in Kapila et al. (2001), Saurel et al. (2008), Grove (2010), Lund (2012) to cite a few. In this approach, each phase is considered compressible and governed by an appropriate equation of state (EOS), as examined in Section 3. The multiphase mixture evolves in velocity, pressure and temperature equilibrium. Temperature equilibrium is justified in the present context as heat diffusion is considered resulting in temperature continuity at interfaces.

Five chemical species are present in the sodium-water reaction context, present in two thermodynamic phases: liquid and vapor water, liquid and vapor sodium, liquid and vapor soda, hydrogen and nitrogen. Oxygen being absent in the modeling, hydrogen combustion is thus omitted. Indeed, sodium-water explosions have been observed in experiments involving atmosphere made of argon only (Carnevali et al., 2013).

The corresponding flow model reads:

$$\begin{cases} \dfrac{\partial \rho Y^L_{H_2O}}{\partial t} + \mathrm{div}\left(\rho Y^L_{H_2O}\vec{u}\right) = \rho \nu_{H_2O}\left(g^g_{H_2O} - g^L_{H_2O}\right) \\ \dfrac{\partial \rho Y^L_{N_a}}{\partial t} + \mathrm{div}\left(\rho Y^L_{N_a}\vec{u}\right) = \rho \nu_{N_a}\left(g^g_{N_a} - g^L_{N_a}\right) - \dot{\omega}_{SR} \\ \dfrac{\partial \rho Y^L_{N_aOH}}{\partial t} + \mathrm{div}\left(\rho Y^L_{N_aOH}\vec{u}\right) = \rho \nu_{N_aOH}\left(g^g_{N_aOH} - g^L_{N_aOH}\right) + \varphi_{N_aOH}\left(\dot{\omega}_{GR} + \dot{\omega}_{SR}\right) \end{cases} \quad \text{(liquid phase mass balances)}$$

$$\begin{cases} \dfrac{\partial \rho Y^g_{H_2O}}{\partial t} + \mathrm{div}\left(\rho Y^g_{H_2O}\vec{u} + \alpha_g \overrightarrow{F^g_{H_2O}}\right) = -\rho \nu_{H_2O}\left(g^g_{H_2O} - g^L_{H_2O}\right) - \varphi_{H_2O}\left(\dot{\omega}_{GR} + \dot{\omega}_{SR}\right) \\ \dfrac{\partial \rho Y^g_{N_a}}{\partial t} + \mathrm{div}\left(\rho Y^g_{N_a}\vec{u} + \alpha_g \overrightarrow{F^g_{N_a}}\right) = -\rho \nu_{N_a}\left(g^g_{N_a} - g^L_{N_a}\right) - \dot{\omega}_{GR} \\ \dfrac{\partial \rho Y^g_{N_aOH}}{\partial t} + \mathrm{div}\left(\rho Y^g_{N_aOH}\vec{u} + \alpha_g \overrightarrow{F^g_{N_aOH}}\right) = -\rho \nu_{N_aOH}\left(g^g_{N_aOH} - g^L_{N_aOH}\right) \\ \dfrac{\partial \rho Y^g_{H_2}}{\partial t} + \mathrm{div}\left(\rho Y^g_{H_2}\vec{u} + \alpha_g \overrightarrow{F^g_{H_2}}\right) = \varphi_{H_2}\left(\dot{\omega}_{GR} + \dot{\omega}_{SR}\right) \\ \dfrac{\partial \rho Y^g_{N_2}}{\partial t} + \mathrm{div}\left(\rho Y^g_{Air}\vec{u} + \alpha_g \overrightarrow{F^g_{Air}}\right) = 0 \end{cases} \quad \text{(gas phase mass balances)} \quad (2.1)$$

$$\frac{\partial \rho \vec{u}}{\partial t} + \mathrm{div}\left(\rho \vec{u} \otimes \vec{u} + p\bar{\bar{I}}\right) = \rho \vec{g} + \sigma_{N_a}\kappa_{N_a}\overrightarrow{\nabla \alpha^L_{N_a}} + \sigma_{H_2O}\kappa_{H_2O}\overrightarrow{\nabla \alpha^L_{H_2O}} \quad \text{(mixture momentum balance)}$$

$$\frac{\partial \rho E}{\partial t} + \mathrm{div}\left[(\rho E + p)\vec{u} + \alpha_g \overrightarrow{q_M} + \overrightarrow{q_T}\right] = \rho \vec{g}.\vec{u} + \sigma_{N_a}\kappa_{N_a}\overrightarrow{\nabla \alpha^L_{N_a}}.\vec{u} + \sigma_{H_2O}\kappa_{H_2O}\overrightarrow{\nabla \alpha^L_{H_2O}}.\vec{u} \quad \text{(mixture energy balance)}$$

The flow model being quite unusual, some details are needed. The main flow variables are detailed hereafter:

- ρ ($= \sum_{k=1}^{N} \rho Y_k$ with $N = 8$) denotes the two-phase mixture density.
- Mass fractions with respect to the two-phase mixture are denoted by Y_k;
- $\vec{u}$ represents the mixture center of mass velocity;
- α_g represents the gas volume fraction. It is defined by $\alpha_g = \rho \sum_{k=4}^{N} \frac{Y_k}{\rho_k(p,T)}$, where p and T respectively represent the mixture pressure and temperature. Relation between ρ_k, p and T is given in Section 3.

- E denotes the total energy ($E = e + \frac{1}{2}|\vec{u}|^2$, with $e = \sum_{k=1}^{N} Y_k e_k$ the mixture internal energy).

The various physicochemical effects considered are detailed in the following subsections.

2.1 Thermal diffusion

The present model dealing with mixtures in mechanical and thermal equilibrium is suitable for the computation of interfaces when heat conduction is present and related boundary layers resolved, as will be done in the computations. The energy equation flux is thus augmented by heat diffusion effects ($\overrightarrow{q_T} = -\left(\sum_{k=1}^{3} (\alpha_k \lambda_k) + \alpha_g \overline{\lambda_g} \right) \overrightarrow{\nabla T}$), where λ_k represents the thermal conductivity of the phase or species k, given in the Table 2.1. The gas phase thermal conductivity is defined by $\overline{\lambda_g} = \frac{1}{2}\left(\sum_{k>3} x_k \lambda_k + 1 \Big/ \sum_{k>3} (x_k / \lambda_k) \right)$ (Kee et al., 1989), where x_k represents the molar fraction of the species k in the gas mixture,

$x_k = \frac{y_k / W_k}{\sum_{i>3} y_i / W_i}$.

In this definition,

- y_k denotes the mass fraction of species k in the gas mixture ($y_k = Y_k / Y_g$, with $Y_g = 1 - Y^L_{H_2O} - Y^L_{N_a} - Y^L_{N_aOH}$ the gas mixture mass fraction with respect to the two-phase mixture).
- W_k represents the molar mass of the species k (Table 2.1).

	Liquid water	Liquid sodium	Liquid soda	Water vapor	Sodium vapor	Soda vapor	Hydrogen	Nitrogen
$\lambda_k\,(w/m/K)$	0.6071	70	0.68	16×10^{-3}	45×10^{-3}	16×10^{-3}	187×10^{-3}	28.2×10^{-3}
$W_k\,(g/mol)$	18	22.98	40	18	22.98	40	2	28

Table 2.1: Thermal conductivities and molar masses of the fluids considered for the SWR (Sodium-Water Reaction) modelling.

2.2 Mass diffusion within the gas phase

The modelling of mass diffusion follows the lines of Giovangigli (2012) for gas mixtures with mild modifications as two phases are present in the present context. In System (2.1), the mass diffusion flux of a given gaseous species k reads,

$$\vec{F_k} = C \frac{1}{p}\left(y_k \overrightarrow{\nabla p} - \overrightarrow{\nabla p_k} \right), \qquad (2.2)$$

where C represents a diffusion coefficient (taken constant and equal to $10^{-4}\,kg/m/s$ in the present application) and p_k denotes the partial pressure. The associated energy flux reads:

$\overrightarrow{q_M} = \sum_{k>3} h_k \vec{F_k}$,

with h_k the enthalpy of species k.

As molecular diffusion is considered in the gas phase only, the diffusion flux $\vec{F_k}$ is weighted by the volume fraction α_g in the mass balance equations.

Compatibility of (2.2) with the second law of thermodynamics is examined in Appendix A.

The molecular diffusion flux (2.2) can also be expressed as,

$\overrightarrow{F_k} = C\frac{1}{p}\left((y_k - x_k)\overrightarrow{\nabla p} - p\overrightarrow{\nabla x_k}\right)$,

where x_k denotes the molar fraction of the gas species k. In the specific context of the SWR (Sodium-Water Reaction), most of the evolution is quasi-isobaric and the term $\overrightarrow{\nabla x_k}$ is the driving diffusion force.

2.3 Phase transition

Phase transition between a liquid and its vapor is a phenomenon that tends to relax the Gibbs free energy of the phases towards equilibrium. In System (2.1) related terms appear in the right-hand side of the mass balance equations as,

$\rho\nu_i\left(g_{i,vap} - g_{i,liq}\right)$,

where $g_{i,vap}$ (resp. $g_{i,liq}$) denotes the vapor phase (resp. liquid phase) Gibbs free energy of a given species i (water, sodium or soda). By definition, $g_i = h_i - Ts_i$, where s_i denotes the entropy of species i. Besides, the parameter ν_i controls the rate at which thermodynamic equilibrium is reached. In the present context of SWR, phase change is controlled by heat and mass diffusion, that are orders of magnitude slower than thermochemical relaxation. It is therefore appropriate to consider that ν_i tends to infinity, meaning that local thermodynamic equilibrium is considered.

For a given species, local thermodynamic equilibrium implies,

$g_{vap}\left(p^*, T^*\right) = g_{liq}\left(p^*, T^*\right)$.

It directly translates to the following relationship:

$p_{partial}^{vap} = x_{vap}^* p^* = p_{sat}\left(T^*\right)$.

Combined with the mixture specific volume and internal energy definitions, the algebraic system to solve to determine the equilibrium state $\left(p^*, T^*, Y_{liq}^*, Y_{vap}^*\right)$ reads,

$$\begin{cases} p_{partial}^{vap} = x_{vap}^* p^* = p_{sat}\left(T^*\right) \\ v = Y_{liq}^* v_{liq}\left(p^*, T^*\right) + Y_{vap}^* v_{vap}\left(p^*, T^*\right) + \sum_{\substack{k\neq liq \\ k\neq vap}} Y_k v_k\left(p^*, T^*\right) \\ e = Y_{liq}^* e_{liq}\left(p^*, T^*\right) + Y_{vap}^* e_{vap}\left(p^*, T^*\right) + \sum_{\substack{k\neq liq \\ k\neq vap}} Y_k e_k\left(p^*, T^*\right) \\ Y_{vap}^* = 1 - Y_{liq}^* - \sum_{\substack{k\neq liq \\ k\neq vap}} Y_k \end{cases} \quad (2.3)$$

with $x_{vap}^* = \frac{Y_{vap}/W_{vap}}{\sum_{k\geq 4} Y_k/W_k}$.

The resolution method for this non-linear system follows Chiapolino et al. (2017a) and is summarized in Section 4.

2.4 Surface reaction

System (2.1) involves surface reaction occurring at the liquid sodium surface through production terms $\dot{\omega}_{SR}$. Water vapor is produced at the liquid water-gas interface and diffused through the gas film to the sodium surface. As molecular diffusion is a slow process compared to the kinetics of the surface reaction, this one is considered instantaneous.

A single global reaction between liquid sodium and water vapor is considered:

$$N_a^{(L)} + H_2O^{(v)} \rightarrow NaOH^{(L)} + \frac{1}{2}H_2^{(g)}. \quad (2.4)$$

This reaction is exothermic,

$\Delta H_{SR}^0 = -177\text{kJ/mol}$.

Liquid soda reference energy is adjusted to fit this reaction heat release. In this aim Reaction (2.4) is expressed in mass terms:

$$1\text{kg}_{N_a^{(L)}} + \frac{W_{H_2O}}{W_{N_a}}\text{kg}_{H_2O^{(v)}} \rightarrow \frac{W_{N_aOH}}{W_{N_a}}\text{kg}_{N_aOH^{(L)}} + \frac{W_{H_2}}{2W_{N_a}}\text{kg}_{H_2^{(g)}},$$

i.e.,

$$1\,\text{kg}_{N_a^{(L)}} + \varphi_{H_2O}\,\text{kg}_{H_2O^{(v)}} \rightarrow \varphi_{N_aOH}\,\text{kg}_{N_aOH^{(L)}} + \varphi_{H_2}\,\text{kg}_{H_2^{(g)}},$$

with $\varphi_{H_2O} = 0.78$, $\varphi_{N_aOH} = 1.74$ and $\varphi_{H_2} = 0.04$.

As shown in Section 3 dedicated to the thermodynamic closure of System (2.1), each phase is governed by the Noble-Abel – Stiffened-Gas (NASG) (Le Metayer and Saurel, 2016) equation of state (EOS) with the enthalpy defined as,

$$h_k(p,T) = c_{p,k}T + b_k p + q_k,$$

where constants $b^g_{H_2O}$ and $b^g_{H_2}$ are zero.

With this definition the heat of reaction at atmospheric conditions (p_0, T_0) reads,

$$\Delta H^0_{SR} = \varphi_{N_aOH}\left(c_{p,N_aOH^{(L)}}T_0 + b^L_{N_aOH}p_0 + q^L_{N_aOH}\right) + \varphi_{H_2}\left(c_{p,H_2^{(g)}}T_0 + q^g_{H_2}\right) - \varphi_{H_2O}\left(c_{p,H_2O^{(g)}}T_0 + q^g_{H_2O}\right) - \left(c_{p,N_a^{(L)}}T_0 + b^L_{N_a}p_0 + q^L_{N_a}\right)$$

$$\equiv -7.702\text{MJ/kg}_{N_a}$$

The reference energy of hydrogen is zero $\left(q^g_{H_2} = 0\right)$. Those of both liquid sodium and water vapor are known, as shown in Section 3. The reference energy of liquid soda is consequently determined to respect ΔH^0_{SR} :

$$q^L_{N_aOH} = \frac{-7.702\text{MJ/kg}_{N_a} - \left(\varphi_{N_aOH}c_{p,N_aOH^{(L)}} + \varphi_{H_2}c_{p,H_2^{(g)}} - \varphi_{H_2O}c_{p,H_2O^{(g)}} - c_{p,N_a^{(L)}}\right)T_0 - \varphi_{N_aOH}b^L_{N_aOH}p_0 + b^L_{N_a}p_0 + \varphi_{H_2O}q^g_{H_2O} + q^L_{N_a}}{\varphi_{N_aOH}}$$

$$= -3.974\times10^6\ \text{J/kg}$$

Details regarding production terms $\dot{\omega}_{SR}$ are given in Section 4, this reaction being considered instantaneous.

2.5 Gas phase reaction

System (2.1) involves gas phase reaction through production terms $\dot{\omega}_{GR}$.

A single global gas reaction is considered between water vapor and sodium vapor. It produces liquid soda and gas hydrogen:

$$N_a^{(v)} + H_2O^{(v)} \rightarrow N_aOH^{(L)} + \frac{1}{2}H_2^{(g)} \qquad (2.5)$$

The associated heat release is, $\Delta H^0_{GR} = -281\text{kJ/mol}$.

Chemical kinetics data for the reaction between water and sodium vapors seem absent in the literature. An estimate is given in Takata et al. (2009) via the transition state theory, but in the author's knowledge, experimental data are lacking for its validation.

Two options have thus been considered:

a) Instantaneous reaction. The gas phase reaction is assumed very fast compared to the other physical processes in presence, such as mass diffusion. Details regarding the computation of production terms $\dot{\omega}_{GR}$ in this specific context are given in Section 4.

b) Finite rate kinetics. Considering delayed gas reaction allows mixing of water and sodium vapors present in the gas film before reaction triggering. If gas premixing is intense enough, a premixed flame is expected instead of a diffusion one. Finite-rate chemistry is addressed through the following mass production rates,

$$\begin{cases} \dot{\omega}_{GR}^{N_a} = -W_{N_a} k_f [N_a][H_2O] \\ \dot{\omega}_{GR}^{H_2O} = -W_{H_2O} k_f [N_a][H_2O] \\ \dot{\omega}_{GR}^{N_aOH} = W_{N_aOH} k_f [N_a][H_2O] \\ \dot{\omega}_{GR}^{H_2} = \frac{1}{2} W_{H_2} k_f [N_a][H_2O] \end{cases},$$

where $[k] = \frac{\rho_g Y_k}{W_k}$ denotes the molar concentration of the species k in the gas phase, with $\rho_g = \frac{\rho Y_g}{\alpha_g}$.

Arrhenius-type law is used for the reaction rate k_f,

$$k_f(T) = k_0 T^n e^{-E_a/RT}, \quad (2.6)$$

with k_0 the pre-exponential factor, n a positive exponent, E_a the activation energy and $R = 8.314\ J/mol/K$ the gas constant. Reaction rate constants have been chosen so that the reaction is stiff when the threshold temperature of 1250 K is reached:

$k_0 = 9 \times 10^{20}$, $n = 2$, $E_a = 5.75 \times 10^5\ J/mol$.

This modeling is quite arbitrary but allows qualitative analysis of premixing effects. The following subsection presents another effect able to enhance gas premixing effects.

2.6 Turbulent diffusion

Experiments carried out by Daudin (2015), Daudin et al. (2018) have highlighted the turbulent nature of the gaseous film separating both sodium and water liquids. Many gas bubbles of various sizes separate the sodium drop from the liquid water surface (Figure 2.1) rendering the gas film highly turbulent.

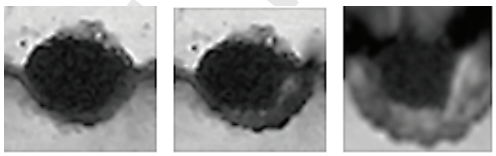

Figure 2.1: Gas bubbles present in the gas film separating the sodium drop and the liquid water surface - VIPERE experiments carried out at CEA Cadarache (Daudin 2015, Daudin et al. 2018). The gas film is consequently more a mixing zone than a film defined by two sharp interfaces.

Presence of these small bubbles are expected to enhance water and sodium vapors mixing prior to gas reaction runaway when finite rate kinetics is considered (option **b** of the previous subsection). Considering such turbulent mixing with liquid-gas interfaces could be addressed through DNS with the present flow model (System 2.1) but would require tremendous spatial and temporal resolution. For simplicity reasons, turbulent effects are considered qualitatively through amplified molecular diffusion within the gas film.

The mass diffusion coefficient C from the relationship (2.2) is modified as follows,

$$C\left(Y_{H_2O}^L, Y_{H_2O}^g, Y_{N_a}^g\right) = C_0\left(1 + a Y_{H_2O}^{g\,2} Y_{N_a}^{g\,2}\right), \quad (2.7)$$

where $a = 3000$ represents an amplification parameter.

2.7 Gravity effects

Gravity effects, particularly important for buoyancy effects and gas layer size selection, are considered through $\rho\vec{g}$ in the momentum balance equation, where $\vec{g}$ denotes gravity acceleration. The right-hand side of the energy equation involves the power of the same force ($\rho\vec{g}.\vec{u}$).

2.8 Surface tension effects

Capillary forces have been added as well and are present at the liquid water-gas interface through the term $\sigma_{H_2O}\kappa_{H_2O}\overrightarrow{\nabla\alpha^L_{H_2O}}$ and at the liquid sodium-gas interface $\sigma_{N_a}\kappa_{N_a}\overrightarrow{\nabla\alpha^L_{N_a}}$, with σ_{H_2O} and σ_{N_a} the surface tension coefficients taken constant in the present study ($\sigma_{H_2O}=0.07\text{N/m}$ and $\sigma_{N_a}=0.2\text{N/m}$). The volume fractions are defined by $\alpha^L_{H_2O}=\dfrac{\rho Y^L_{H_2O}}{\rho^L_{H_2O}(p,T)}$ and $\alpha^L_{N_a}=\dfrac{\rho Y^L_{N_a}}{\rho^L_{N_a}(p,T)}$. The local interface curvatures are denoted by κ_{H_2O} and κ_{N_a}, and defined as,

$$\kappa_{H_2O}=-\text{div}\left(\frac{\overrightarrow{\nabla\alpha^L_{H_2O}}}{\left|\overrightarrow{\nabla\alpha^L_{H_2O}}\right|}\right),\qquad \kappa_{N_a}=-\text{div}\left(\frac{\overrightarrow{\nabla\alpha^L_{N_a}}}{\left|\overrightarrow{\nabla\alpha^L_{N_a}}\right|}\right).$$

The present modelling of surface tension effects corresponds to the Brackbill et al. (1992) approach, extended to compressible fluids in Perigaud and Saurel (2005).

2.9 Some properties of flow model (2.1)

System (2.1) satisfies the fundamental principles of physics such as mixture mass, mixture momentum and mixture energy conservation. The model is also thermodynamically consistent, i.e. it fulfils the second law of thermodynamics,

$$\frac{\partial\rho s}{\partial t}+\text{div}\left(\rho s\vec{u}+\alpha_g\sum_{k>3}s_k\vec{F_k}-\frac{\lambda_c}{T}\overrightarrow{\nabla T}\right)=\begin{pmatrix}\dfrac{\rho\nu_{H_2O}(g^g_{H_2O}-g^L_{H_2O})^2}{T}+\dfrac{\rho\nu_{N_a}(g^g_{N_a}-g^L_{N_a})^2}{T}\\ +\dfrac{\alpha_g p}{TC}\displaystyle\sum_{k>3}\left(v_k\left|\vec{F_k}\right|^2\right)+\dfrac{\lambda_c}{T^2}\left|\overrightarrow{\nabla T}\right|^2\\ \underbrace{-\dfrac{|\dot\omega_{RS}|}{T}\Delta G^0_{SR}}_{<0}\underbrace{-\dfrac{|\dot\omega_{RG}|}{T}\Delta G^0_{GR}}_{<0}\end{pmatrix}\geq 0,$$

where $s=\sum_{k=1}^{N}Y_k s_k$ represents the mixture entropy and ΔG^0 represents the Gibbs free energy reaction.

In the absence of diffusive effects, source and capillary terms, it can be shown easily that the system is hyperbolic with wave speeds u, $u-c$, $u+c$. The mixture sound speed definition is given in Le Martelot et al. (2014). Note that its precise knowledge is useless as it is always slightly lower than the Wood (1930) sound speed given by,

$$\frac{1}{\rho c_w^2}=\sum_{k=1}^{N}\frac{\alpha_k}{\rho_k c_k^2},$$

useful for numerical resolution of the system.

Last, the equations are Galilean invariant. In the absence of non-condensable gases, chemical reactions and mass diffusion, the compressible flow model of Le Martelot et al. (2014) for boiling flows is recovered.

3. Thermodynamic closure

The mixture equation of state is a consequence of the following algebraic system:

$$\begin{aligned}&T=T_k,\ \forall k\in\{1,\dots,N\}\\ &v=1/\rho=\sum_{k=1}^{N}Y_k v_k(p,T)\\ &p=p_k,\ \forall k\in\{1,\dots,N\}\\ &e=\sum_{k=1}^{N}Y_k e_k(p,T)\end{aligned}\qquad(3.1)$$

In this system, fluids are in pressure and temperature equilibrium, but each one occupies its own volume or its own volume fraction. This is very different of the well-known Dalton's law, used for gas

mixtures, which assumes that each gas species occupies the entire volume and that the pressure is the sum of the partial pressures:

$$T_g = T_k \ ; \qquad V_g = V_k \ ; \qquad p_g = \sum_{k=1}^{N} p_k \ ; \qquad e_g = \sum_{k=1}^{N} Y_k e_k \ .$$

For ideal gases, molecules are free to move throughout the entire volume. But for liquid/gas systems phases cannot occupy the whole volume. In this context of so-called "separate phases", the mixture EOS is a consequence of System (3.1). It therefore requires knowledge of the EOS governing each phase, to express $v_k(p,T)$ and $e_k(p,T)$.

3.1. Equations of state of the pure phases

Each fluid thermodynamics is considered through the NASG EOS (Le Metayer and Saurel, 2016). Its caloric formulation reads,

$$p_k(v_k,e_k) = \frac{(\gamma_k - 1)(e_k - q_k)}{(v_k - b_k)} - \gamma_k p_{\infty,k} \ .$$

The term $(\gamma_k - 1)(e_k - q_k)$ represents thermal agitation while $(v_k - b_k)$ represents short range repulsive effects. The term $\gamma_k p_{\infty,k}$, present in liquids and solids, corresponds to the attractive effects responsible of condensed matter cohesion.

The associated thermal equation of state is built from Maxwell's rules. It reads,

$$T_k(v_k,p_k) = \frac{(v_k - b_k)(p_k + p_{\infty,k})}{(\gamma_k - 1)c_{v,k}} \ .$$

For a given phase k, determination of parameters γ_k, b_k, $p_{\infty,k}$, $c_{v,k}$ and q_k is based on the experimental phase diagram. The coefficients of a liquid phase and its vapor are coupled in order to reproduce the experimental saturation curves, latent heat and saturation pressure following the method given in Le Metayer and Saurel (2016). Limitations appear in the vicinity of the critical point, but this is not relevant in the SWR context.

The NASG parameters of the different fluids are listed in the Table (3.1).

	γ_k	$b_k\ (m^3/kg)$	$p_{\infty,k}\ (Pa)$	$c_{v,k}\ (J/kg/K)$	$q_k\ (J/kg)$	$q'_k\ (J/kg/K)$
Liquid water	1.19	6.61×10^{-4}	7028×10^{5}	3610	-1177788	0
Liquid sodium	1.28	9.168×10^{-4}	7452×10^{5}	995	-256257	0
Liquid Soda	1.14	4.55×10^{-4}	1500×10^{6}	1830	-3.974×10^{6}	0
Water vapor	1.47	0	0	955	2077616	14317
Sodium vapor	1.62	0	0	250	4.624×10^{6}	5220
Soda vapor	1.45	0	0	900	1.712×10^{6}	7420
Hydrogen	1.41	0	0	10160	0	0
Nitrogen	1.4	0	0	920	0	0

Table 3.1: NASG parameters of the various fluids considered for the SWR modelling.

Parameters of liquid water and its vapor are given in Le Metayer and Saurel (2016). Regarding sodium, saturation curves are given in Fink and Leibowitz (1995) and the various EOS parameters (vapor and liquid) are determined from these data. The corresponding theoretical curves are compared to the reference ones in Figure 3.1.

The soda heat capacity at constant pressure ($c^L_{p,N_aOH} = 2100\ J/kg/K$) is taken constant and adjusted at $T \approx 1000\ K$ from Chase (1998). The liquid soda density as a function of temperature at atmospheric

pressure is given in Daubert et al. (1994) and leads to the determination of parameters c^L_{v,N_aOH}, $b^L_{N_aOH}$ and p^L_{∞,N_aOH}. The value of $\gamma^L_{N_aOH}$ is then obtained as $c^L_{p,N_aOH} = \gamma^L_{N_aOH} c^L_{v,N_aOH}$. Finally, it should be noted that the liquid soda reference energy $q^L_{N_aOH}$ is determined to agree with the surface reaction heat release, as addressed in Section 2.4.

Reference data such as latent heat of vaporization of soda and soda saturation pressure are reported in Lide (2009) and have been used to determine soda vapor NASG parameters, from those of liquid soda, given in Table 3.1.

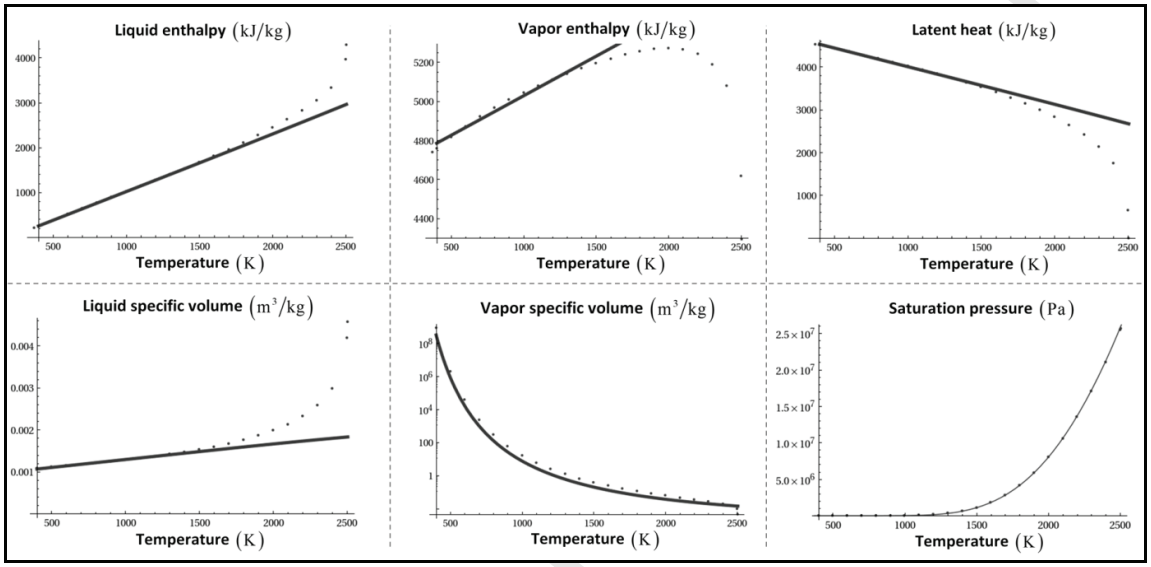

Figure 3.1: Reference (points) and theoretical (lines) sodium saturation curves. Very good agreement is observed in the temperature range $[300\text{K} - 1500\text{K}]$. This range is wide enough for SWR studies as explosions typically occur when the sodium temperature reaches about 1000K (Daudin, 2015).

3.2. Mixture equation of state

From System (3.1) and having in hands the NASG EOS for each phases and fluids, two relationships enable mixture temperature computation. From the mixture specific volume definition $v = \sum_{k=1}^{N} Y_k v_k(p,T)$, the mixture temperature is obtained as:

$$T(p,v) = \frac{v - \sum_{k=1}^{N} Y_k b_k}{\sum_{k=1}^{N} \frac{Y_k c_{v,k} (\gamma_k - 1)}{p + p_{\infty,k}}}. \tag{3.2}$$

From the mixture internal energy definition $e = \sum_{k=1}^{N} Y_k e_k(p,T)$ another relation for the mixture temperature is obtained:

$$T(p,e) = \frac{e - \sum_{k=1}^{N} Y_k q_k}{\sum_{k=1}^{N} Y_k c_{v,k} + \sum_{k=1}^{N} \frac{Y_k c_{v,k} (\gamma_k - 1) p_{\infty,k}}{p + p_{\infty,k}}}. \tag{3.3}$$

Combining (3.2) with (3.3), the mixture pressure becomes solution of the following equation,

$$f(p) = \sum_{k=1}^{N} \frac{Y_k c_{v,k} (\gamma_k - 1)}{p + p_{\infty,k}} \left(\frac{e - \sum_{k=1}^{N} Y_k q_k}{v - \sum_{k=1}^{N} Y_k b_k} - p_{\infty,k} \right) - \sum_{k=1}^{N} Y_k c_{v,k}. \tag{3.4}$$

Its resolution requires an iterative method such as Newton's one.
The flow model (2.1) with thermodynamic closure (3.4) form a closed system of equations. Its numerical resolution poses many challenges that are addressed in the following section.

4. Numerical method

Numerical resolution of the System (2.1) is done in the DALPHADT© code based on both structured and unstructured meshes [www.rs2n.eu]. The first step of the numerical method consists in solving the Riemann problem in the presence of both gravity and surface tension effects (Section 4.1). Their accurate computation is mandatory in the present context, as the gas film width selection occurs in situations close to mechanical equilibrium. Numerical approximation of heat and mass diffusive effects is then addressed in Sections 4.2 and 4.3. The interface sharpening method of Chiapolino et al. (2017b) is then adapted to the present diffuse interface flow model, slightly different to the one of that reference. Stiff source terms solvers are then addressed for phase transition in Section 4.6 and instantaneous chemical reactions in Sections 4.7 and 4.8.

4.1 Mechanical equilibrium Riemann solver with gravity and surface tension

Accurate computation of gravity effects is of primary importance in the present context as gas layer width selection, directly linked to the various diffusive effects present in the flame, is closely driven by buoyancy. Insertion of gravity effects in the flux computation, through 'well balanced' Riemann solvers has been the subject of many efforts, such as for example LeVeque (1998), Gosse (2000) and Gallice (2002). In order to avoid numerical errors due to operator splitting, surface tension has also to be considered in the Riemann solver.
In the present section the HLLC solver (Toro et al., 1994) is considered. Both gravity and capillary effects are embedded in the solver, unlike the other source terms (phase transition, chemical reactions). Solver positivity is obviously important (Zhang and Shu, 2011) in the presence of gravity. In the present frame, the resulting solver is genuinely positive, an important property when dealing with material interfaces and large density ratios, as well as sophisticated EOS, as the one given in Section 3.
Let us consider the hyperbolic part of System (2.1):

$$\frac{\partial U}{\partial t}+\mathrm{div}\left[F\right]=0\,, \tag{4.1}$$

with $U=\begin{pmatrix}\rho Y_k\\ \rho\vec{u}\\ \rho E\end{pmatrix}$ and $F=\begin{pmatrix}\rho Y_k\vec{u}\\ \rho\vec{u}\otimes\vec{u}+p\mathrm{I}\\ (\rho E+p)\vec{u}\end{pmatrix}$.

In the HLLC solver three waves are considered:

- The extreme waves speeds S_L and S_R, estimated as (Davis, 1988),

  $S_L=\min\left(\left(\vec{u}.\vec{\eta_f}\right)_L-c_L,\left(\vec{u}.\vec{\eta_f}\right)_R-c_R\right)$

  $S_R=\max\left(\left(\vec{u}.\vec{\eta_f}\right)_L+c_L,\left(\vec{u}.\vec{\eta_f}\right)_R+c_R\right)$,

  with $\vec{\eta_f}$ the unit normal vector of the face f oriented towards the cell R. For the sake of simplicity, normal velocities are denoted by $\left(\vec{u}.\vec{\eta_f}\right)_L\equiv u_L$ and $\left(\vec{u}.\vec{\eta_f}\right)_R\equiv u_R$ in the following.
- The contact discontinuity speed S_M, to determine in the presence of both gravity and capillary effects.

The Rankine-Hugoniot relations through the extreme waves read,

$$\left(F.\vec{\eta_f}\right)_L^*=\left(F.\vec{\eta_f}\right)_L+S_L\left(U_L^*-U_L\right),\qquad \left(F.\vec{\eta_f}\right)_R^*=\left(F.\vec{\eta_f}\right)_R+S_R\left(U_R^*-U_R\right) \tag{4.2}$$

and lead to the usual expressions of pressure in the star regions:

$$p_L^*=p_L+\rho_L\left(u_L-S_L\right)\left(u_L-S_M\right),\qquad p_R^*=p_R+\rho_R\left(u_R-S_R\right)\left(u_R-S_M\right) \tag{4.3}$$

In the frame of the Euler equations pressure equality is ensured through the contact wave condition ($p_L^* = p_R^*$). In the present context, this condition is replaced by another equilibrium condition.

Gravity effects consideration in the HLLC solver

The contact condition requires integration of the equilibrium condition:

$\overrightarrow{\nabla p} = \rho \vec{g}$,

where $\vec{g} = (0, \ -g)^T$ represents the gravity vector.

The equilibrium condition can be rewritten as follows:

$$\begin{cases} \dfrac{\partial p}{\partial x} = 0 \\ \dfrac{\partial p}{\partial y} = -\rho g \end{cases} \tag{4.4}$$

Integration of the second relation is achieved on both sides of face f separating the two cells L and R:

$$\int_{p^*}^{p_R} dp = -\int_{\bar{y}}^{y_R} \rho g dy \Leftrightarrow p_R + \rho_R g y_R = p^* + \rho_R g \bar{y}, \qquad \int_{p_L}^{p^*} dp = -\int_{y_L}^{\bar{y}} \rho g dy \Leftrightarrow p_L + \rho_L g y_L = p^* + \rho_L g \bar{y} \tag{4.5}$$

with p^* the pressure solution of the Riemann problem and $\bar{y}$ the vertical coordinate of the face f center (Figure 4.1).

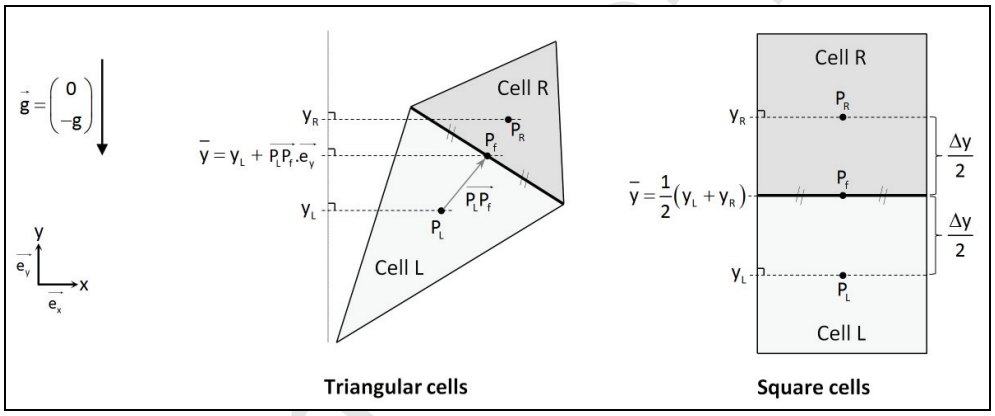

Figure 4.1: Determination of $\bar{y}$ for two mesh types (triangular and cartesian grids). P_L and P_R represent respectively the centers of cells L and R. P_f is the center of face f.

Relations (4.5) are rewritten in the star states as follows:

$$\begin{cases} p_R^* + \rho_R g y_R = p^* + \rho_R g \bar{y} \\ p_L^* + \rho_L g y_L = p^* + \rho_L g \bar{y} \end{cases}, \tag{4.6}$$

where the density variations have been assumed negligible through the acoustic waves.

Combining (4.3) and (4.6) leads to the determination of both contact wave speed S_M and star pressure p^* in the presence of gravity:

$$\begin{cases} S_M = \dfrac{p_R - p_L + \rho_L u_L (S_L - u_L) - \rho_R u_R (S_R - u_R) + \rho_R g (y_R - \bar{y}) - \rho_L g (y_L - \bar{y})}{\rho_L (S_L - u_L) - \rho_R (S_R - u_R)} \\ p^* = \dfrac{(p_R + \rho_R (u_R - S_R) u_R) \rho_L (u_L - S_L) - (p_L + \rho_L (u_L - S_L) u_L) \rho_R (u_R - S_R)}{\rho_L (u_L - S_L) - \rho_R (u_R - S_R)} + \dfrac{\rho_L (u_L - S_L) \rho_R g (y_R - \bar{y}) - \rho_R (u_R - S_R) \rho_L g (y_L - \bar{y})}{\rho_L (u_L - S_L) - \rho_R (u_R - S_R)} \end{cases} \tag{4.7}$$

Efficiency of the method is illustrated on the following test case. Let's consider a 10m height tank, the lower half tank being filled with water and the upper one with air. The initial pressure in the entire vessel is the atmospheric one. The considered mesh is coarse (100 cells) to highlight differences between the conventional splitting method and the present one, where gravity effects

are embedded in the Riemann solver. In this test, only hydrodynamic and gravity effects are considered. Corresponding results are shown in the Figure 4.2.

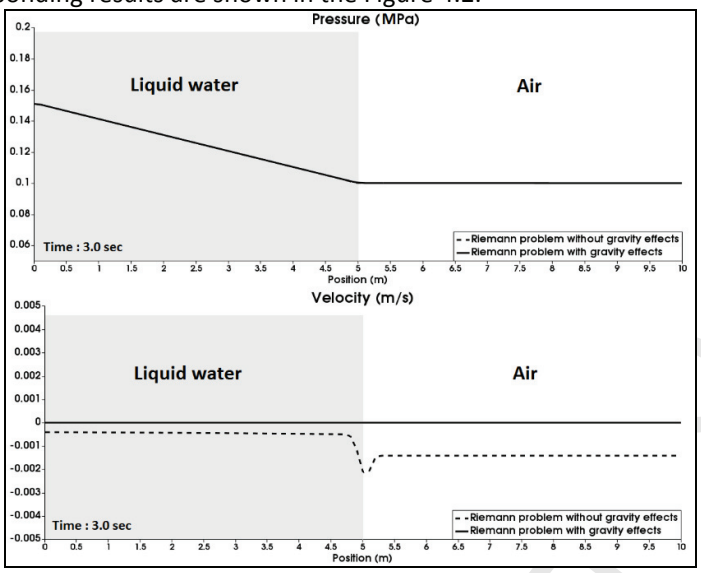

Figure 4.2. Mechanical equilibrium of a water column in air. The conventional Godunov method with source terms splitting is compared to the present one, where gravity terms are embedded in the HLLC solver. Both methods compute correct pressure field, but the new method only is free of parasitic velocity when equilibrium is reached. Computed results are shown at time 3 s.

The equilibrium state is perfectly matched with the new method. Surface tension effects are now considered.

Capillary effects consideration in the HLLC solver

In the presence of surface tension, pressure equality through the contact wave ($p_L^* = p_R^*$) is replaced by the following condition (Perigaud and Saurel, 2005, Garrick et al., 2017):

$p_R^* - p_L^* = \sigma\kappa\left(\alpha_{liq,R} - \alpha_{liq,L}\right)$,

with $\kappa = \frac{1}{2}\left(\kappa_L + \kappa_R\right)$.

This contact relation guarantees agreement with the Laplace law. Typical examples and verifications are illustrated in Figure 4.3.

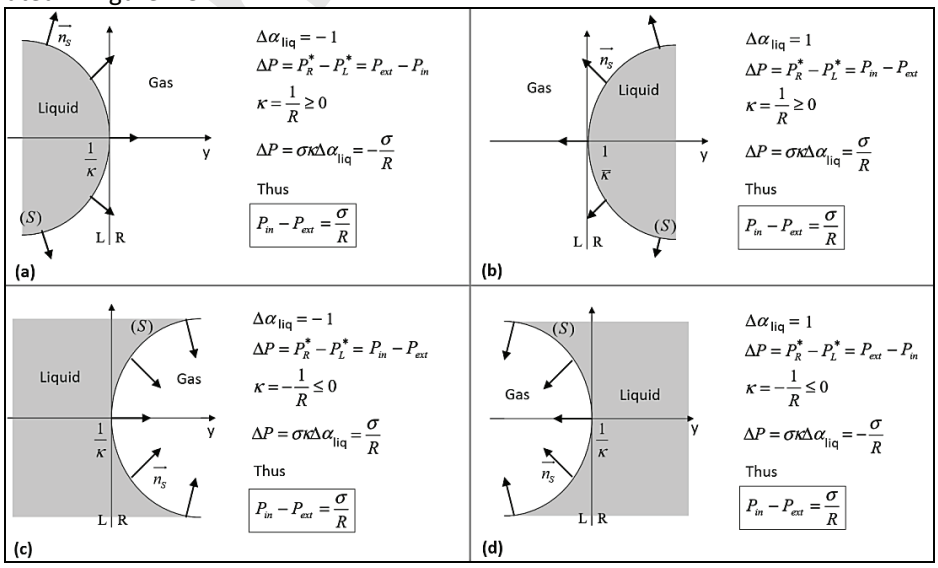

Figure 4.3: The various configurations that may occur at a curved interface separating a liquid and a gas.

The star pressure p^* is then obtained as:

$$p^* = p_R^* - \sigma\kappa\alpha_{liq,R} = p_L^* - \sigma\kappa\alpha_{liq,L} \tag{4.8}$$

Combining (4.3) and (4.8) implies:

$$\begin{cases} S_M = \dfrac{p_R - p_L + \rho_L u_L (S_L - u_L) - \rho_R u_R (S_R - u_R) - \sigma\kappa\left(\alpha_{liq,R} - \alpha_{liq,L}\right)}{\rho_L (S_L - u_L) - \rho_R (S_R - u_R)} \\ p^* = \dfrac{\left(p_R + \rho_R (u_R - S_R) u_R\right)\rho_L (u_L - S_L) - \left(p_L + \rho_L (u_L - S_L) u_L\right)\rho_R (u_R - S_R)}{\rho_L (u_L - S_L) - \rho_R (u_R - S_R)} - \sigma\kappa \dfrac{\alpha_{liq,R}\rho_L (u_L - S_L) - \alpha_{liq,L}\rho_R (u_R - S_R)}{\rho_L (u_L - S_L) - \rho_R (u_R - S_R)} \end{cases} \tag{4.9}$$

The first relation of System (4.9) corresponds to the one given in Garrick et al. (2017).

When both gravity and surface tension effects are present, the estimate of S_M is consequently,

$$S_M = \frac{p_R - p_L + \rho_L u_L (S_L - u_L) - \rho_R u_R (S_R - u_R) + \rho_R g\left(y_R - \bar{y}\right) - \rho_L g\left(y_L - \bar{y}\right) - \sigma\kappa\left(\alpha_{liq,R} - \alpha_{liq,L}\right)}{\rho_L (S_L - u_L) - \rho_R (S_R - u_R)} \tag{4.10}$$

The primitive variable vector in the star states is thus fully determined and the solution sampling is done to compute the flux F of System (4.1).

For example, in the subsonic case and for $S_M > 0$, the flux solution of the Riemann problem on a given face f along the face normal vector $\vec{\eta_f}$ reads,

$$\left(F.\vec{\eta_f}\right)^* = \begin{pmatrix} \rho_L^* Y_{k,L}^* S_M \\ \rho_L^* S_M \vec{u_L^*} + \left[p_L^* + \rho_L g\left(y_L - \bar{y}\right)\right]\vec{\eta_f} \\ \left[\rho_L^* E_L^* + p_L^* + \rho_L g\left(y_L - \bar{y}\right)\right] S_M \end{pmatrix}, \text{ with } \begin{cases} Y_{k,L}^* = Y_{k,L} \\ \rho_L^* = \rho_L \dfrac{u_L - S_L}{S_M - S_L} \\ E_L^* = E_L + \dfrac{p_L u_L - \left[p_L^* + \rho_L g\left(y_L - \bar{y}\right)\right] S_M}{\rho_L (u_L - S_L)} \\ \vec{u_L^*} = S_M \vec{\eta_f} + \vec{u_L^\perp} \end{cases}$$

In these formulas, p_L^* is given by (4.3) and S_M is defined by (4.10). Besides, $\vec{u_L^\perp} = \vec{u_L} - u_L \vec{\eta_f}$ denotes the velocity vector tangential to the face f.

The correction of p_L^* by the gravity term $\rho_L g\left(y_L - \bar{y}\right)$ is a consequence of the pressure profile linearity, characteristic of gravity effects. Let us consider the specific case of a state close to the equilibrium one described by (4.6) in the absence of surface tension. Any small velocity fluctuation modifying the sign of S_M would lead to an unacceptable variations between p_L^* and p_R^* if the correction term $\rho_L g\left(y_L - \bar{y}\right)$ was not considered to compute the flux F^*. This correction therefore allows to preserve the mechanical equilibrium condition (4.6).

Contrary to the gravity case, no explicit correction of the pressure p_L^* due to capillary effects appears in the flux F computation. Indeed, a pressure discontinuity appears in (4.8).

The present Riemann solver with surface tension requires local curvature computation and consequently volume fraction gradients computation, as addressed in the next section.

4.2 Volume fraction gradients and local curvature

The CSF method recalled in Section 2.8 has been already considered with compressible fluids and diffuse interfaces (Perigaud and Saurel, 2005, Le Martelot et al., 2014, Garrick et al. 2017, Schmidmayer et al., 2017) but extra difficulties appear in the present application as a result of interface sharpening through the method presented in the subsequent Section 4.5. Computation of the local curvature becomes problematic. The approach used in the present work is gradually described in the following.

Volume fraction gradient determination at cell centers

A robust and accurate method for the computation of volume fraction gradients is based on least squares approximation. It is based on multiple Taylor expansions around cell center P_i and a cloud of neighboring cells indexed by j:

$$\begin{aligned}\alpha_j &= \alpha_i + \overrightarrow{P_iP_j}.\overrightarrow{e_x}\frac{\partial\alpha_i}{\partial x} + \overrightarrow{P_iP_j}.\overrightarrow{e_y}\frac{\partial\alpha_i}{\partial y} + O\left(\left\|\overrightarrow{P_iP_j}\right\|^2\right) \\ &= \alpha_i + \Delta x_{ij}\frac{\partial\alpha_i}{\partial x} + \Delta y_{ij}\frac{\partial\alpha_i}{\partial y} + O\left(\left\|\overrightarrow{P_iP_j}\right\|^2\right)\end{aligned}, \tag{4.11}$$

where $\overrightarrow{e_x}$ and $\overrightarrow{e_y}$ denote the unit vectors of the Cartesian basis.

Using (4.11) with a set of N neighbors $(j \in \{1,\dots,N\})$ results in the following system,

$$\begin{pmatrix} \omega_1\Delta x_{i1} & \omega_1\Delta y_{i1} \\ . & . \\ . & . \\ . & . \\ \omega_N\Delta x_{iN} & \omega_N\Delta y_{iN} \end{pmatrix} \begin{pmatrix} \frac{\partial\alpha_i}{\partial x} \\ \frac{\partial\alpha_i}{\partial y} \end{pmatrix} = \begin{pmatrix} \omega_1(\alpha_1 - \alpha_i) \\ . \\ . \\ . \\ \omega_N(\alpha_N - \alpha_i) \end{pmatrix} \Leftrightarrow AX = B,$$

with $\omega_j = \frac{1}{\Delta x_{ij}^2 + \Delta y_{ij}^2}$.

Weights ω_j allows to control numerical instabilities (division by small numbers) when the mesh is skewed. In two dimensions, a minimum of two neighboring elements is necessary to solve the system. When the number of available neighbors is greater than two, then the system is over-determined. A classical way to solve this over-determined system is to multiply both sides of $AX = B$ by the transpose matrix. A square system is obtained: $A^TAX = A^TB$, and the solution reads, $X = (A^TA)^{-1}A^TB$.

It is possible to consider direct neighbors only of the considered cell (direct stencil) or both direct and indirect neighbors (extended stencil). Both configurations are schematized in Figure 4.4.

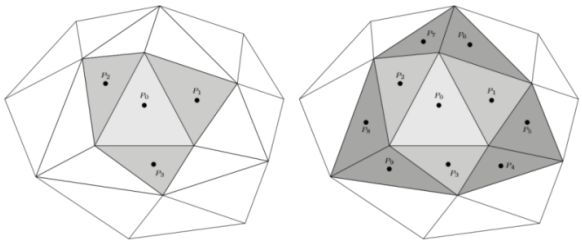

Figure 4.4: Schematic representation of direct and indirect neighbors of the considered cell on an unstructured mesh made of triangles. On the left, only direct neighbors are colored (direct stencil). On the right, both direct and indirect neighbors are colored (extended stencil).

In the following, extended stencil is retained for accuracy reasons. The liquid volume fraction gradient being determined, the next step consists in computing the interface curvature at each cell center.

Interface curvature determination at cell centers

The local curvature has been defined in (2.8) and requires volume fraction gradients computation, as detailed previously. However, as the liquid volume fraction is sharpened with the method given in Section 4.5 some difficulties emerge. The liquid volume fraction gradient is not regular enough to compute curvature accurately.

To circumvent this difficulty, a color function C_{liq} with smooth profile is introduced. It is built at each time step with the following initial data,

$$\begin{cases} \text{If } \alpha_{liq} \geq 0.5, \ C_{liq} = 1 \\ \text{Otherwise}, \ C_{liq} = 0 \end{cases}$$

An iterative type diffusion operator is then used as,

$$C_{liq,i}^{n+1} = \frac{S_i C_{liq,i}^n + \sum_{k=1}^{N_{Neigh}} S_k C_{liq,k}^n}{S_i + \sum_{k=1}^{N_{Neigh}} S_k},$$

with N_{Neigh} the number of direct neighbors of the cell i and S_i the surface of the cell i.

Using this operator during 5 iterations results in a diffuse profile on approximatively 5 cells. The corresponding color function is shown in Figure 4.5 in the specific case of a 2D liquid drop.

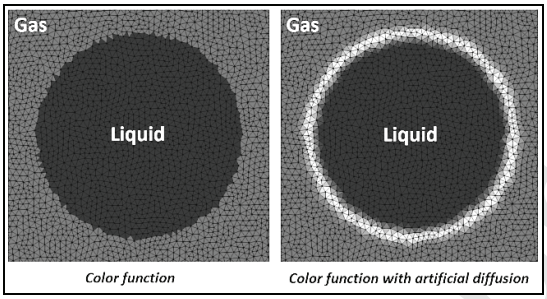

Figure 4.5: Color function with a liquid drop surrounded by air on an unstructured mesh, with and without numerical smearing.

The diffused color function is therefore a good candidate for curvature computation. The latter is then computed as:

$$\kappa = -\mathrm{div}\left(\frac{\overrightarrow{\nabla C_{liq}}}{\left|\overrightarrow{\nabla C_{liq}}\right|}\right).$$

In two-dimension the local interface curvature at a cell center i reads,

$$\kappa_i = -\frac{\left(\frac{\partial C_{liq,i}}{\partial x}\right)^2 \frac{\partial^2 C_{liq,i}}{\partial y^2} - 2\frac{\partial C_{liq,i}}{\partial x}\frac{\partial C_{liq,i}}{\partial y}\frac{\partial^2 C_{liq,i}}{\partial x \partial y} + \left(\frac{\partial C_{liq,i}}{\partial y}\right)^2 \frac{\partial^2 C_{liq,i}}{\partial x^2}}{\left|\overrightarrow{\nabla C_{liq,i}}\right|^3}. \quad (4.12)$$

This expression involves color function gradient components at cell centers, as well as color function Hessian matrix components. Computation of these terms is achieved with the help of the least-squares method previously detailed and used twice. First with the cell center color function as argument and second with resulting gradient components that become arguments of the Hessian matrix approximation.

Curvature computation oscillations

To assess curvature computation method, a test with a simple circular interface is considered. By definition it is the inverse of the radius. Let us consider a 5mm radius sodium drop with curvature $200\,\mathrm{m}^{-1}$.

The curvature computed with (4.12) is shown in Figure 4.6, for two types of meshes (triangular cells and square ones). Whatever the mesh considered, the computed curvature oscillates along the interface. It is thus necessary to correct its computation. This issue has been reported by many authors (Renardy and Renardy 2002, Garrick et al. 2017) for example.

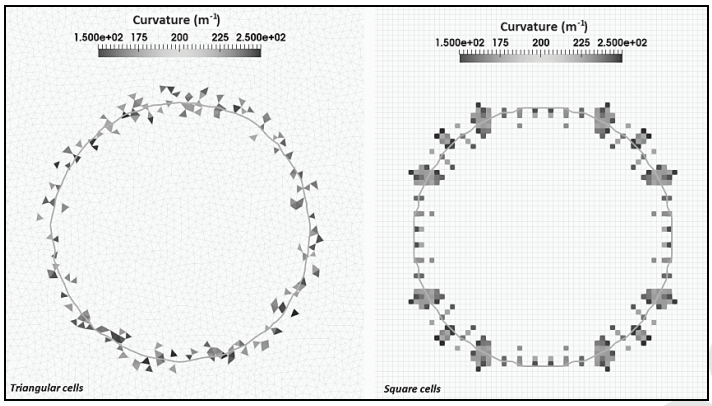

Figure 4.6: Computed curvature for a circular interface – Two types of meshes are considered – Only cells with curvature close to the theoretical value are shown. Large variations are present.

Curvature correction

Curvature computation is accurate at cells located on the interface, i.e. at cells for which the color function is close to 0.5. The method adopted consists in extending the value of the curvature computed in these cells to the surrounding ones, with the help of a weighted diffusion operator (Garrick et al., 2017). This is done with the following iterative method, used at each time step,

$$\kappa_i^{n+1} = \frac{\omega_i \kappa_i^n + \sum_{k=1}^{N_{Neigh}} \omega_k \kappa_k^n}{\omega_i + \sum_{k=1}^{N_{Neigh}} \omega_k},$$

with $\omega_k = S_k \left[C_{liq,k} \left(1 - C_{liq,k} \right) \right]^2$ a Gaussian weighting function centered on the interface where $C_{liq,k} \approx 0.5$. This correction is illustrated in Figure 4.7 with the same 5 mm radius sodium drop test case as before.

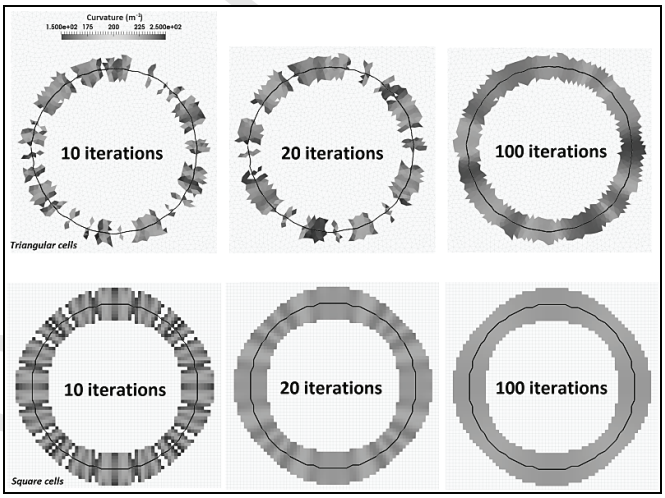

Figure 4.7: The circle curvature is computed with the two different types of meshes (triangles on top, squares on bottom). For each mesh type, varying numbers of iterations in the curvature diffusion method are used.

Accuracy of the curvature computation increases with the number of iterations of the diffusion method. Convergence towards exact curvature appeared faster with square cells. It also appeared important to limit correction steps, especially in zones where the interface is highly curved, as neighboring cells values would corrupt the correct value of κ. In the various 2D computations that are presented hereafter and in Section 6, Cartesian grids are used with typically 10 iterations. In the present application smooth interfaces are mainly considered and the method appeared appropriate.

Validation

The overall method with capillary Riemann solver and regularized curvature is validated on the following example. A 5mm radius sodium drop is placed on liquid water surface. The rest of the domain is made of ambient air. The various fluids are transported at velocity 0.5m/s to the right. Only hydrodynamic and surface tension effects of sodium are considered in these computations. The pressure jump, initially imposed inside the drop, is determined with the Laplace law:

$$p_{N_a} = p_{atm} + \frac{\sigma}{R} = 10^5 + \frac{1.5}{5\times10^{-3}} = 100300 \text{ Pa}.$$

Here, $\sigma = 1.5 \text{N.m}^{-1}$ corresponds to a large value, in order to assess robustness of the numerical method. The aim of computations shown in the Figure 4.8 is to check pressure jump preservation during drop motion.

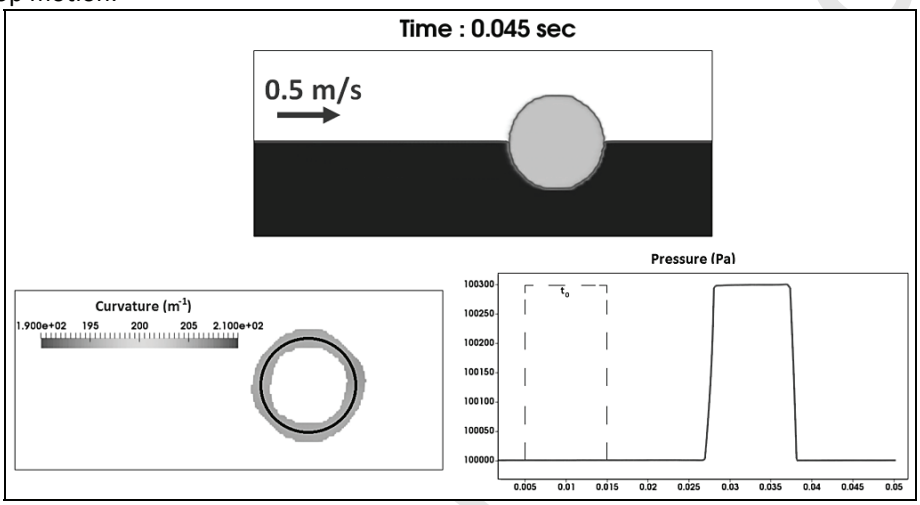

Figure 4.8: The initial pressure jump is preserved during drop transport, validating the capillary solver.

Numerical treatment of extra physical effects is addressed in the subsequent subsections.

4.3 Thermal diffusion

As mentioned in Section 2.1 thermal diffusion flux reads,

$$\overrightarrow{q_T} = -\lambda_M \overrightarrow{\nabla T},$$

$$\text{with } \lambda_M = \sum_{k=1}^{3} (\alpha_k \lambda_k) + \alpha_g \overline{\lambda_g}. \tag{4.13}$$

For a given cell boundary, the numerical method is based on both temperature and diffusion flux continuity.

The normal component of the flux expressed at left of face f reads,

$$q_{T,L} = -\lambda_{M,L} \frac{T_I - T_L}{\Delta_L},$$

where T_I represents the face/interface temperature to be determined, T_L the temperature at cell center L and $\Delta_L = \left|\overrightarrow{P_L P_f}.\overrightarrow{\eta_f}\right|$ the distance normal to the face from the cell center, as shown in Figure 4.9. $\lambda_{M,L}$ denotes the mixture thermal conductivity defined by (4.13) and involves volume fractions of the different phases determined within the cell L.

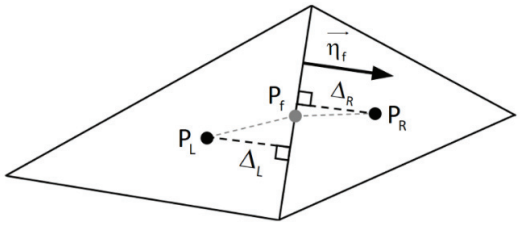

Figure 4.9: Representation of the distances Δ_L and Δ_R that appear in the thermal diffusion flux discretization. P_L and P_R represent respectively the centers of cells L and R. P_f is the center of the face f.

Equality of normal flux components implies:

$$-\lambda_{M,L}\frac{T_I - T_L}{\Delta_L} = -\lambda_{M,R}\frac{T_R - T_I}{\Delta_R}.$$

It leads to the determination of T_I:

$$T_I = \frac{\lambda_{M,L}\Delta_R T_L + \lambda_{M,R}\Delta_L T_R}{\lambda_{M,L}\Delta_R + \lambda_{M,R}\Delta_L}. \tag{4.14}$$

Once T_I is computed the normal flux component is computed with $q_{T,L}$ or $q_{T,R}$ indifferently.

4.4 Mass diffusion terms

The computation of the mass diffusion flux follows the lines of the previous section. The mass diffusion flux is recalled hereafter:

$$\vec{F_k} = C\frac{1}{p}\left((y_k - x_k)\vec{\nabla p} - p\vec{\nabla x_k}\right)$$

It can be rewritten as follows:

$$\vec{F_k} = \vec{F_{k,1}} + \vec{F_{k,2}}$$

with $\vec{F_{k,1}} = C\frac{1}{p}(y_k - x_k)\vec{\nabla p}$ and $\vec{F_{k,2}} = -C\vec{\nabla x_k}$.

The flux $\vec{F_{k,2}}$ is projected onto the normal of the face and its continuity implies,

$$-C_L\frac{x_{k,I} - x_{k,L}}{\Delta_L} = -C_R\frac{x_{k,R} - x_{k,I}}{\Delta_R}.$$

The interface molar fraction is thus determined as,

$$x_{k,I} = \frac{C_L\Delta_R x_{k,L} + C_R\Delta_L x_{k,R}}{C_L\Delta_R + C_R\Delta_L}. \tag{4.15}$$

It enables straightforward computation of the $\vec{F_{k,2}}$ normal component. Flux $\vec{F_{k,1}}$ is now considered.

The interface molar fraction being known, the interface mass fraction is directly obtained as,

$$y_{k,I} = \frac{W_k x_{k,I}}{\sum_{i>3} W_i x_{i,I}}. \tag{4.16}$$

Continuity of normal component of $\vec{F_{k,1}}$ implies,

$$\frac{C_L(y_{k,I} - x_{k,I})}{p_I}\frac{p_I - p_L}{\Delta_L} = \frac{C_R(y_{k,I} - x_{k,I})}{p_I}\frac{p_R - p_I}{\Delta_R}.$$

The interface pressure p_I is consequently deduced as,

$$p_I = \frac{C_L\Delta_R p_L + C_R\Delta_L p_R}{C_L\Delta_R + C_R\Delta_L}. \tag{4.17}$$

The discrete form $F_{k,dis}$ of the normal component of the mass diffusion flux thus reads,

$$F_{k,dis} = \frac{C_L\left(y_{k,I} - x_{k,I}\right)}{p_I}\frac{p_I - p_L}{\Delta_L} - C_L\frac{x_{k,I} - x_{k,L}}{\Delta_L},$$

with $x_{k,I}$, $y_{k,I}$ and p_I defined respectively by (4.15), (4.16) and (4.17).

Last, the associate discrete energy flux $Q = \sum_k h_k F_k$ requires the knowledge of both interface temperature T_I given by (4.14) and interface pressure p_I, since $h_k(p,T) = c_{p,k}T + b_k p + q_k$.

Interface sharpening is now addressed to reduce interfaces numerical smearing.

4.5 Interface sharpening

MUSCL type reconstruction is used, as detailed in Chiapolino et al. (2017b). As well-known numerical diffusion smears interfaces over several mesh points even when compressive limiters, such as Superbee (Roe, 1985) are used. To overcome this difficulty the Overbee limiter of Chiapolino et al. (2017b) is used. It consists in a compressive limiter valid for linearly degenerate fields only and transport of Heaviside function, such as volume fraction separating two fluids.

The method is adapted to the flow model (2.1) by adding extra equations with respect to the volume fractions,

$$\frac{\partial \alpha_k}{\partial t} + \vec{u}.\overrightarrow{\nabla \alpha_k} = 0, \tag{4.18}$$

where k represents liquid water $(H_2O)_L$, liquid sodium $(N_a)_L$, liquid soda $(N_aOH)_L$ and multi-component gas (g).

The Overbee limiter is used for these equations only. Denoting by ϕ_f the ratio of two gradients adjacent to a cell face ($\phi_f = (\alpha_{i+1} - \alpha_i)/(\alpha_i - \alpha_{i-1})$ in the simplified case of structured mesh), extrapolation from the cell center to the face is done through limited gradients through the formula:

$\theta(\phi_f) = max\left[0, min(2\phi_f, 2)\right]$.

This limiter is used at interfaces only, that are detected as,

$\alpha_k^n \alpha_j^n > \varepsilon$, with $j \neq k$.

According to numerical experiments, $\varepsilon = 10^{-2}$ is a fair choice (Chiapolino et al., 2017b).

The other flow variables present in System (2.1) are computed with the same method, except that the Minmod limiter is used.

System (4.18) is solved during each time step of the hyperbolic solver. Sharpening volume fractions with the help of the Overbee limiter results in enhanced accuracy in the various fluxes computation and consequently in sharpened mixture density and mass fractions.

But adding System (4.18) to System (2.1) corresponds to an overdetermined system. At the end of the time step all variables must be compatible and this is done by resetting the various volume fractions. With the help of the computed equilibrium pressure p_{eq} and temperature T_{eq} given by (3.4) and (3.3), based on mass fractions (and not volume fractions) the volume fractions are reset as:

-For liquids,

$$\alpha_k = \frac{\rho Y_k}{\rho_k\left(p_{eq}, T_{eq}\right)}, \forall k \leq 3.$$

-For the multicomponent gas mixture (made of 5 species),

$$\alpha_g = \rho \sum_{k=4}^{8} \frac{Y_k}{\rho_k\left(p_{eq}, T_{eq}\right)}.$$

The method is illustrated on the simple 1D advection test of Figure 4.4 with data relevant to SWR situations. Let us consider a 1D 32cm long tube with an interface separating two fluids with nearly pure liquid water on the left and nearly pure air on the right. The flow variables are uniform in the whole domain,

$$\begin{cases} u^0 = 0.1 \text{m/s} \\ p^0 = 0.1 \text{MPa} \\ T^0 = 300 \text{K} \end{cases},$$

except the mass and volume fractions, as well as mixture density that are discontinuous at x=0.05 m at initial time. Three computations are compared at the same time in Figure 4.10. The accuracy gain observed on the interface capture is noticeable with Overbee.

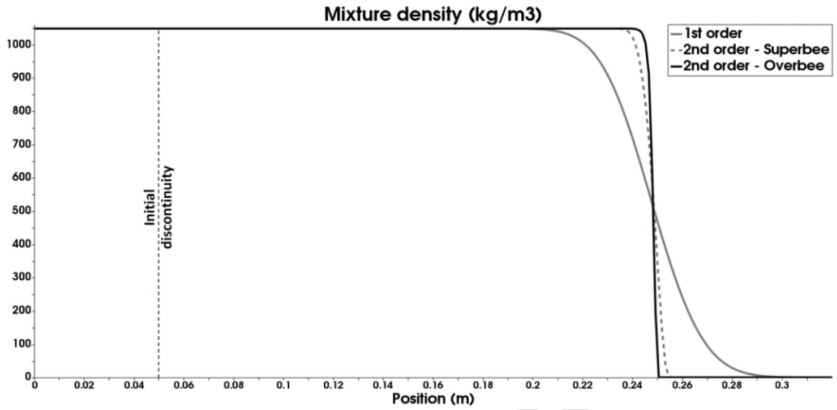

Figure 4.10: Comparison between Superbee and Overbee limiters for the advection of a liquid-gas interface at low speed – Mesh: 240 cells – CFL=0.8 – Final time: 1.98s. As the CFL is based on the sound speed more than 3 600 000-time steps are required to reach final time.

Subsections 4.6 to 4.8 detail the numerical treatment of the various source terms involved in SWR modeling. Conventional source terms splitting is considered in the following.

4.6 Stiff phase transition solver

The non-linear system (2.3) has to be solved to determine the thermodynamic equilibrium state $\left(p^*, T^*, Y_{liq}^*, Y_{vap}^*\right)$ for a given liquid and its vapor. For this purpose, an iterative algorithm as the one given in Le Metayer et al. (2013) can be used. However, the thermochemical relaxation solver of Chiapolino et al. (2017a) is preferred as it manages transitions from mixtures to pure fluids easily, is simple to implement and is faster.

The method summarizes as follows:

- **Check for total evaporation ($Y_{liq}^* \to \varepsilon$)**

  The limit case $Y_{liq}^* \to \varepsilon$ is considered (typically $\varepsilon = 10^{-7}$). Pressure and temperature are determined using the mixture equation of state given in Section 3.2. In addition, the vapor partial pressure is computed.

  If $T > T_{sat}\left(p_{partial}^{vap}\right)$, the solution is $Y_{liq}^* = Y_{min} = 10^{-7}$ and $Y_{vap}^* = 1 - Y_{min} - \sum_{\substack{k \neq liq \\ k \neq vap}} Y_k$.

- **If the liquid phase "liq" is present in sufficient proportions thermodynamic equilibrium is computed**

  Three approximate expressions of Y_{vap}^* are determined:

  - One from the mixture specific volume definition,

$$Y_{Liq}^m(p,T) = \frac{v - \left(1 - \sum_{\substack{k \neq liq \\ k \neq vap}} Y_k\right) v_{vap}(p,T) - \sum_{\substack{k \neq liq \\ k \neq vap}} Y_k v_k(p,T)}{v_{liq}(p,T) - v_{vap}(p,T)},$$

  yielding,

$$Y_{vap}^{m}(p,T) = 1 - Y_{liq}^{m}(p,T) - \sum_{\substack{k\neq liq \\ k\neq vap}} Y_k \ .$$

- Another one from the mixture internal energy definition:

$$Y_{liq}^{e}(p,T) = \frac{e - \left(1 - \sum_{\substack{k\neq liq \\ k\neq vap}} Y_k\right) e_{vap}(p,T) - \sum_{\substack{k\neq liq \\ k\neq vap}} Y_k e_k(p,T)}{e_{liq}(p,T) - e_{vap}(p,T)},$$

Yielding,

$$Y_{vap}^{e}(p,T) = 1 - Y_{liq}^{e}(p,T) - \sum_{\substack{k\neq liq \\ k\neq vap}} Y_k \ .$$

- A last one from the relationship $p_{partial}^{vap} = p_{sat}(T^*)$,

$$Y_{vap}^{sat}(p,T) = \frac{p_{sat}(T) W_{vap}}{p - p_{sat}(T)} \sum_{\substack{k>3 \\ k\neq vap}} Y_k / W_k \ .$$

The approximate mass fraction Y_{vap}^{*} at equilibrium that is retained is the one that produces the minimum variation, provided that the three associated mass transfers are of the same sign.
Let us introduce,

$$\begin{cases} r_1 = \left(Y_{vap}^{m} - Y_{vap}\right)\left(Y_{vap}^{e} - Y_{vap}\right) \\ r_2 = \left(Y_{vap}^{m} - Y_{vap}\right)\left(Y_{vap}^{sat} - Y_{vap}\right) \end{cases}$$

where Y_{vap} is the initial mass fraction resulting of the hyperbolic step.

- If $r_1 < 0$ or $r_2 < 0$, no mass transfer is considered: $Y_{vap}^{*} = Y_{vap}$
- Otherwise the minimum mass transfer is used.

It means,

$$Y_{vap}^{*} = Y_{vap} + \mathrm{sgn}\left[Y_{vap}^{m} - Y_{vap}\right] \times \mathrm{Min}\left[\left|Y_{vap}^{m} - Y_{vap}\right|, \left|Y_{vap}^{e} - Y_{vap}\right|, \left|Y_{vap}^{sat} - Y_{vap}\right|\right].$$

This treatment is reminiscent of TVD type schemes and associated gradient limiters, that are converted in the present frame to source terms limiters.
As several liquids are present in SWR situations special care is needed. Phase transition of water, sodium and soda are treated separately (in three successive steps):

- The relaxation solver is used first with liquid water and its vapor. This step is done assuming that the other gas species (sodium vapor, soda vapor, hydrogen and nitrogen) are frozen and considered as non-condensable ones. In the same way, liquid sodium and liquid soda are considered frozen.
- The relaxation solver is used secondly with liquid sodium and its vapor. The other gas species (water vapor, soda vapor, hydrogen and nitrogen) are frozen during this step, as well as liquid water and liquid soda.
- The relaxation solver is used last with liquid soda and its vapor. The other gas species (water vapor, sodium vapor, hydrogen and nitrogen) are frozen during this step, as well as liquid water and liquid sodium.

Consequently, considering several liquids and associated vapors doesn't introduce extra difficulty.

4.7 Surface reaction

The surface reaction expressed in mass terms is recalled hereafter:

$$1\,kg_{N_a^{(L)}} + \varphi_{H_2O}\,kg_{H_2O^{(v)}} \rightarrow \varphi_{N_aOH}\,kg_{N_aOH^{(L)}} + \varphi_{H_2}\,kg_{H_2^{(g)}},$$

with $\varphi_{H_2O} = 0.78$, $\varphi_{N_aOH} = 1.74$ and $\varphi_{H_2} = 0.04$.

As this reaction is considered instantaneous its numerical treatment is easy. Its global kinetics is controlled by water vapor mass diffusion in the gas film. The liquid sodium and water vapor are compared first:

- If the water vapor concentration is limitating $\left(\rho Y^g_{H_2O} < \varphi_{H_2O}\rho Y^L_{N_a}\right)$, then the mass increment is computed as,

  $d\omega_{SR} = \dfrac{\rho Y^g_{H_2O}}{\varphi_{H_2O}}$.

- Otherwise $d\omega_{SR} = \rho Y^L_{N_a}$.

The various mass fractions are then updated as,

$\left(\rho Y^L_{N_a}\right)^* = \rho Y^L_{N_a} - d\omega_{SR}$

$\left(\rho Y^g_{H_2O}\right)^* = \rho Y^g_{H_2O} - \varphi_{H_2O} d\omega_{SR}$

$\left(\rho Y^L_{N_aOH}\right)^* = \rho Y^L_{N_aOH} + \varphi_{N_aOH} d\omega_{SR}$

$\left(\rho Y^g_{H_2}\right)^* = \rho Y^g_{H_2} + \varphi_{H_2} d\omega_{SR}$,

the state '*' being the post-reaction one.

4.8 Gas phase reaction

The gas reaction between water vapor and sodium vapor is recalled hereafter:

$N_a^{(v)} + H_2O^{(v)} \rightarrow N_aOH^{(L)} + \dfrac{1}{2}H_2^{(g)}$.

Two options have been considered regarding the gas reaction kinetics in Section 2.5: a) Instantaneous reaction, or, b) Finite rate kinetics.

When the reaction is considered instantaneous (a), its numerical treatment follows the same lines as the surface reaction one:

- If the water vapor concentration is limitating $\left(\rho Y^g_{H_2O} < \varphi_{H_2O}\rho Y^g_{N_a}\right)$, then $d\omega_{GR} = \dfrac{\rho Y^g_{H_2O}}{\varphi_{H_2O}}$,

- Otherwise, $d\omega_{GR} = \rho Y^g_{N_a}$.

The various mass fractions are then updated as,

$\left(\rho Y^g_{N_a}\right)^* = \rho Y^g_{N_a} - d\omega_{GR}$

$\left(\rho Y^g_{H_2O}\right)^* = \rho Y^g_{H_2O} - \varphi_{H_2O} d\omega_{GR}$

$\left(\rho Y^L_{N_aOH}\right)^* = \rho Y^L_{N_aOH} + \varphi_{N_aOH} d\omega_{GR}$

$\left(\rho Y^g_{H_2}\right)^* = \rho Y^g_{H_2} + \varphi_{H_2} d\omega_{GR}$,

the state '*' being the post-reaction one.

With option b) source terms are integrated explicitly with second-order Euler method. The flow solver being explicit, finite rate chemistry given in Section 2.5 (b) is not particularly stiff.

In the following section, effects of the various physical ingredients (phase transition, heat and mass diffusion, surface and volume chemical reactions) are illustrated in 1D spherical tests. A new difficulty appears and is related to the numerical treatment of mass diffusion with numerically diffuse interfaces. Indeed, even if the Overbee limiter reduces numerical diffusion, interfaces are still diffused and need special care when physical mass diffusion is considered.

5. Mass diffusion with diffuse interfaces and effects of chemical reactions – 1D spherical tests

A spherical liquid drop of 1mm radius is set in liquid water. The two liquids are separated by a 2 mm gas layer made of nitrogen at elevated initial temperature. A schematic representation of the configuration under interest is shown in Figure 5.1.

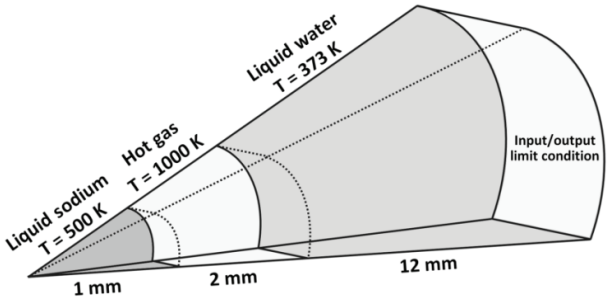

Figure 5.1: 1D configuration relevant to typical SWR situations with a 1 mm radius sodium droplet separated by a gas layer from liquid water. The liquid water domain boundary is treated as an inflow/outflow boundary condition. Precisely liquid water tank at atmospheric pressure and temperature 373 K is imposed at outflow. This outflow may become an inflow if the flow becomes inverted. Details regarding boundary conditions treatment are given in Appendix B.

For a first run, mass diffusion is removed as well as chemical reactions, both in the gas phase and at sodium surface. Surface tension and gravity effects are obviously absent. Therefore, only fluid motion is considered in the presence of heat conduction and phase transition of both water and sodium. Corresponding results are shown in Figure 5.2.

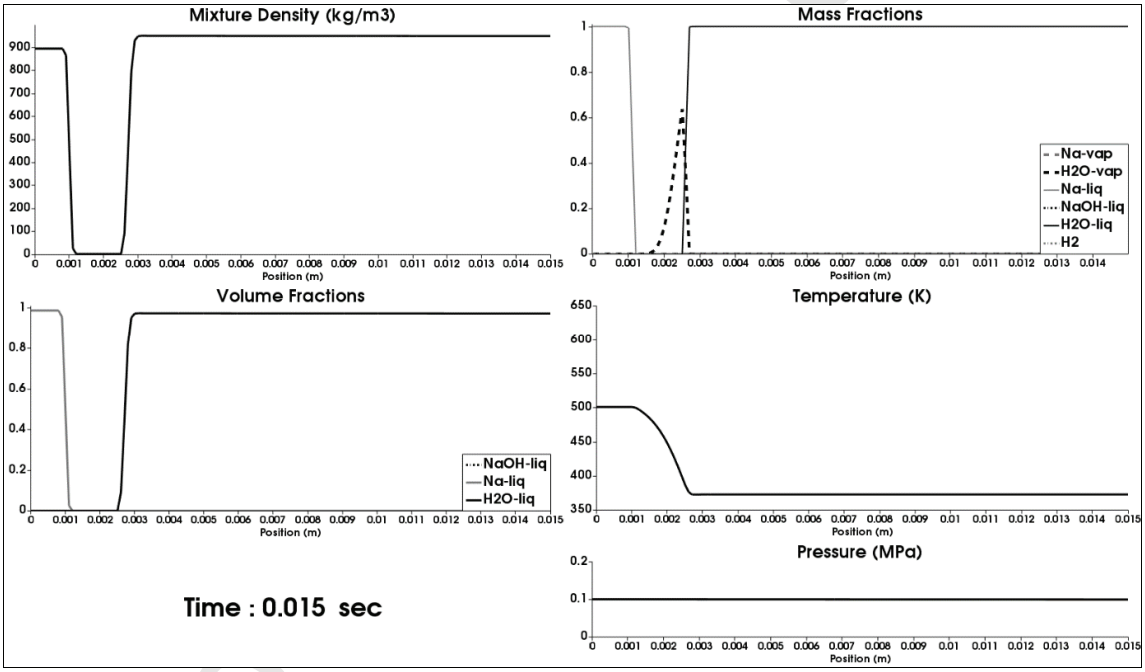

Figure 5.2: 1D reference results related to the 1D SWR test problem of Figure 5.1. Computed results are shown at time 15 ms on a mesh involving 150 cells. Thermal diffusion and phase transition only are present in the flow model (2.1). From the initial situation the gas layer has been cooled and water vapor appears at the interface at right. Both interface motions have been considered but their velocity is not significant in the present example.

In the second run, mass diffusion within the gas phase is considered with constant mass diffusion coefficient: $C = 10^{-4}\,\mathrm{kg/m/s}$ (parameter *a* in Eq. 2.7 characteristic of turbulent diffusion is taken equal to zero). Corresponding results are shown in Figure 5.3 at time 15ms (same as before). The water vapor created at the gas-liquid water interface is now diffused within the multi-component gas until it reaches the liquid sodium-gas interface.

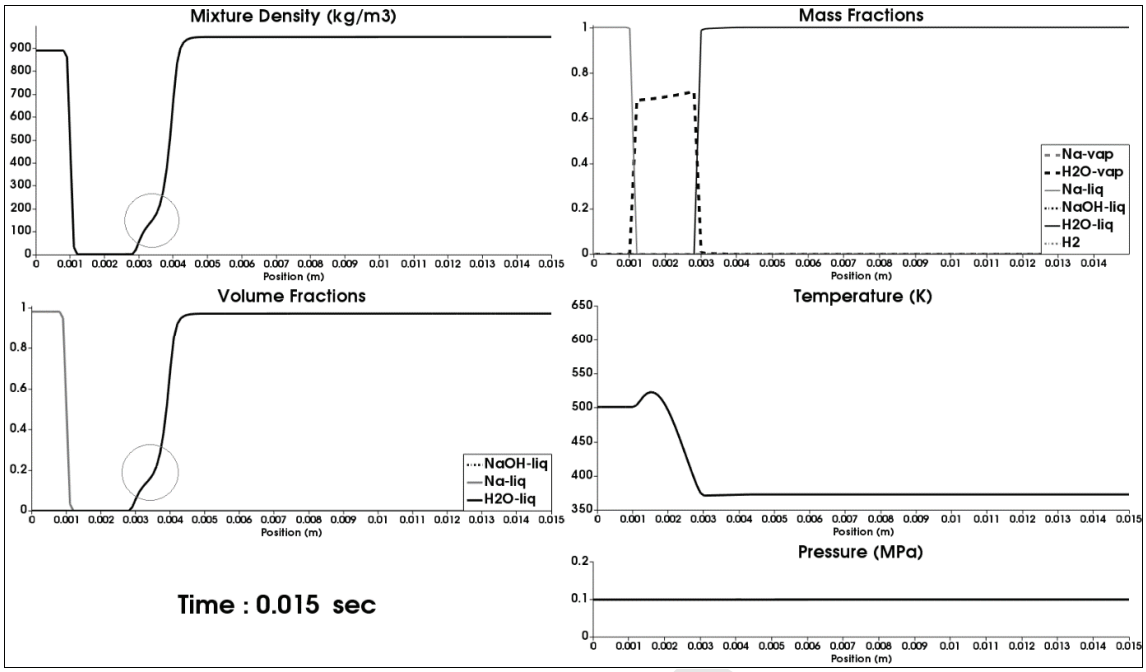

Figure 5.3: 1D computed results related to the 1D SWR test problem of Figure 5.1 in the presence of mass diffusion in addition to fluid motion, heat diffusion and phase transition already considered in the results of Figure 5.2. Same mesh is considered, and the results are shown at the same time. The gas-liquid water interface becomes corrupted as a result of mass diffusion in the numerically diffuse interface.

The interface separating the gas mixture and liquid water becomes unphysical, as clearly visible on the mixture density and volume fraction graphs. This issue results of bad interaction between the mass diffusion flux and the diffuse interface representation.

In the frame of diffuse interface methods, a 'pure' liquid is numerically treated as a mixture with a liquid volume fraction equal to $1-\varepsilon$. The other fluids in minor proportion then share the residue ε. This remark also holds for the related mass and molar fractions. In liquid water, the multi-component gas mass fraction, and in particular the water vapor one, are therefore non-zero. This implies a non-zero water vapor molar fraction (although physically inconsistent) in the liquid water domain. Computation of the related gradient $\overrightarrow{\nabla x_{H_2O}}$ present in the mass diffusion flux is consequently wrong. Weighting the related mass diffusion flux by the gas volume fraction, as done in System (2.1) through the term $\alpha_g \overrightarrow{F^g_{H_2O}}$ is not enough to cure this problem.

To circumvent this difficulty the mass diffusion coefficient C is rendered dependent on the liquid water mass fraction as follows:

$$C\left(Y^L_{H_2O}, Y^g_{H_2O}, Y^g_{N_a}\right) = C_0 H_\chi\left(Y^L_{H_2O}\right)\left(1 + a Y^{g\,2}_{H_2O} Y^{g\,2}_{N_a}\right), \tag{5.1}$$

with $C_0 = 10^{-4}\,kg/m/s$, $a = 0$ (in the present context), $H_\chi\left(Y^L_{H_2O}\right) = \begin{cases} 1, \text{ if } Y^L_{H_2O} \le 0.5+\chi \\ 0, \text{ if } Y^L_{H_2O} > 0.5+\chi \end{cases}$ and $\chi \in]-0.5;0.5[$ a parameter to define. Function $H_\chi\left(Y^L_{H_2O}\right)$ is shown in Figure 5.4.

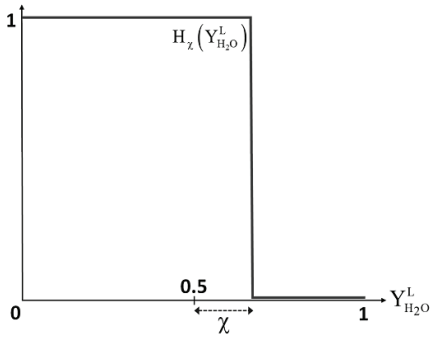

Figure 5.4: Function $H_\chi\left(Y^L_{H_2O}\right)$ used in the mass diffusion coefficient correction.

Function $H_\chi\left(Y^L_{H_2O}\right)$ prevents mass diffusion in quasi-pure liquid zones and prevents interface corruption. $H_\chi\left(Y^L_{H_2O}\right)$ is used only at the gas-liquid water interface. Indeed, at the sodium-gas interface the presence of surface reaction prevents such defect.

With the help of this non-linear diffusion coefficient, the 1D spherical test of Figure 5.1 is rerun. Parameter χ is set to $\chi = 0.2$. Results are shown at the same time as before (15ms) in Figure 5.5, showing correct interface behavior.

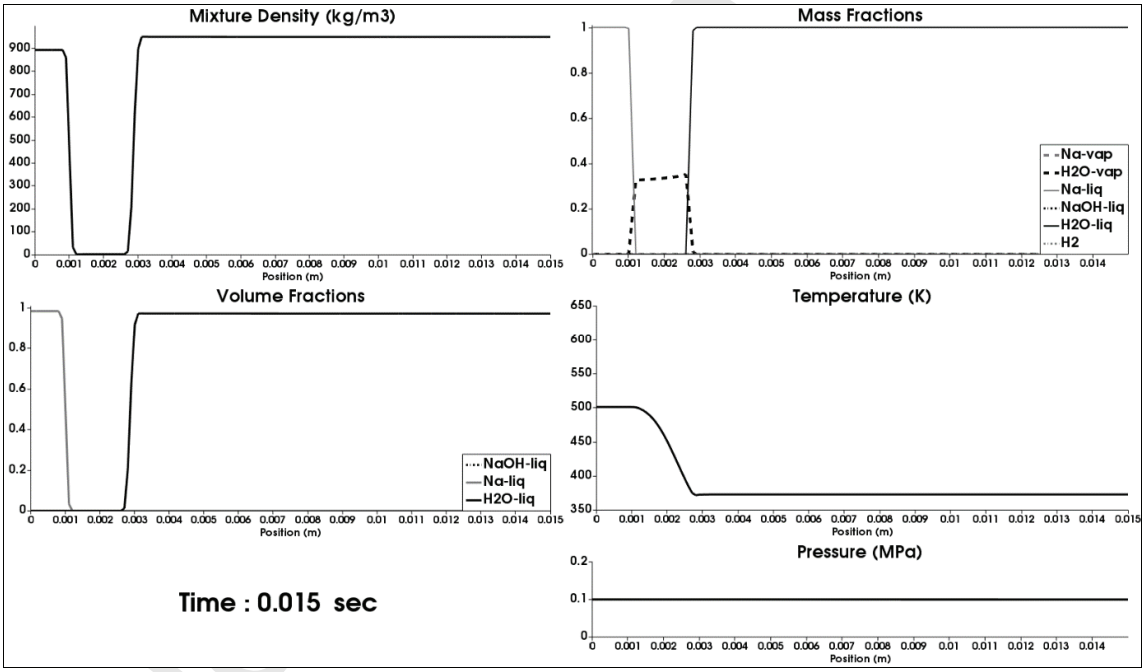

Figure 5.5: 1D computed results related to the 1D SWR test problem of Figure 5.1 in the presence of mass diffusion with non-linear mass diffusion coefficient (5.1). Fluid motion, heat diffusion, phase transition and mass diffusion are considered on the same mesh as in the previous computations, with 150 cells. Sharp liquid water - gas mixture interface is now recovered and mass diffusion in the gas phase is present. Mass diffusion effects appear clearly by comparing the mass fraction graphs of the present figure and the one of Figure 5.2.

Influence of parameter χ

The 1D spherical test of Figure 5.1 is rerun for different values of parameter χ in order to assess its influence on the numerical results. For each test the water vapor mass fraction at the gas-liquid water interface is recorded at different times and shown in Figure 5.6. Influence of parameter χ in the range $[-0.2;0.2]$ appears not noticeable.

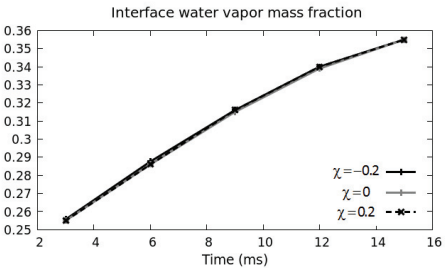

Figure 5.6: The 1D SWR test problem of Figure 5.1 is considered in the presence of fluid motion, heat diffusion, phase transition and mass diffusion. Results obtained with 3 different values of parameter χ are compared. The amount of water vapor produced at the interface does not depend on the parameter χ in the range $[-0.2;0.2]$. Outside this range, differences appear.

The interfacial water vapor mass fraction does not depend on the parameter χ in the range $[-0.2;0.2]$ at least in the present configuration. This parameter is set to $\chi = 0.2$ in the following.

As water vapor now diffuses from the liquid water side to the sodium one it becomes possible to address both surface and volume reactions. To this end the various chemical production terms addressed in Section 4 are used (in the present section, the gas phase reaction is supposed to be instantaneous – option (a) of Section 4.7). Furthermore, it should be noted that phase transition of soda is not considered at this stage, in order to maximize the effects leading to an explosion. Computed results are shown at the same time as before, on the same mesh and are shown in Figure 5.7.

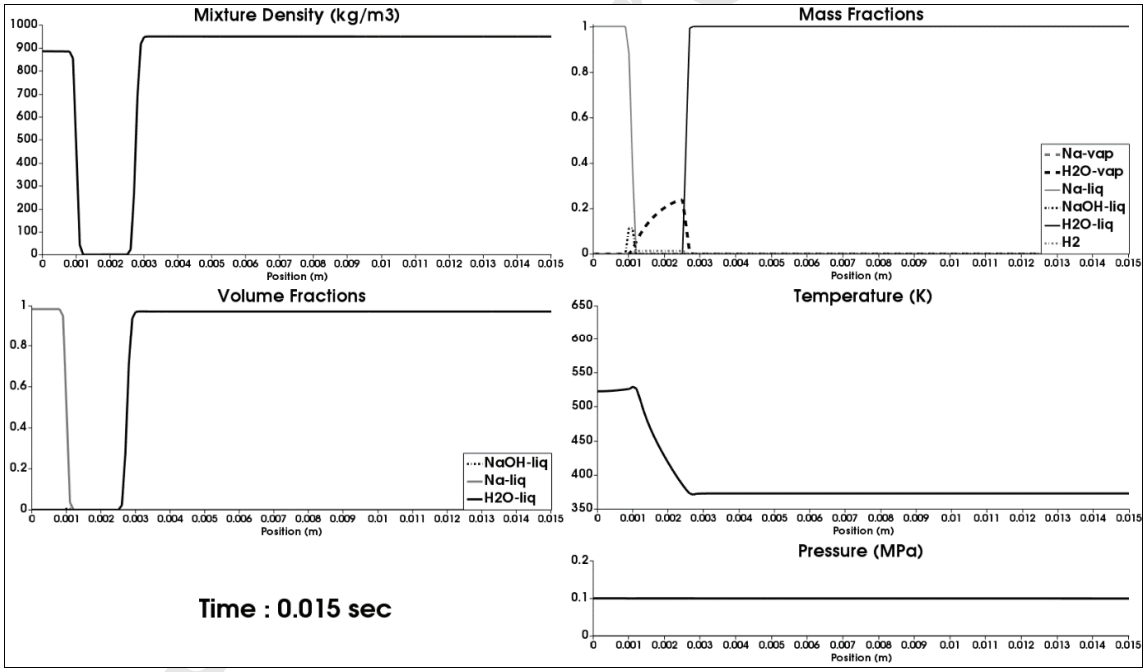

Figure 5.7: 1D computed results related to the 1D SWR test problem of Figure 5.1 in the presence of both surface and gas reactions (both considered instantaneous). Fluid motion, heat diffusion, phase transition of water and sodium species, mass diffusion $(\text{with } \chi = 0.2 \text{ and } a = 0)$ and chemical reactions are considered on the same mesh as in the previous computations, with 150 cells. Results are shown at the same time as before (15ms). The liquid sodium temperature increases, compared to the results of Figure 5.5, as a result of surface reaction combined to heat diffusion.

When the water vapor reaches the liquid sodium-gas interface, surface reaction occurs, generating large soda mass production and local heating. It contributes to both liquid sodium and gas film heating through thermal diffusion. At this level, the interface motion is still imperceptible.

Results at longer times are shown in Figures 5.8 (t=1.503s) and 5.9 (t=2.334s). At time 1.503s, the liquid sodium temperature exceeds 1000K. At this temperature, a larger amount of sodium vapor is produced. This vapor then reacts with the water one through the gas reaction. The gas reaction being more exothermic than the surface one, the temperature locally exceeds 1800K. The mass fraction of liquid soda is locally close to 1 and acts as a barrier between sodium and water vapors present in large quantities. The SWR gas product (hydrogen H_2) is diffused within the gas layer.

In addition, the gas film thickness has significantly increased, compared to the one observed in Figure 5.7, at time t=15ms.

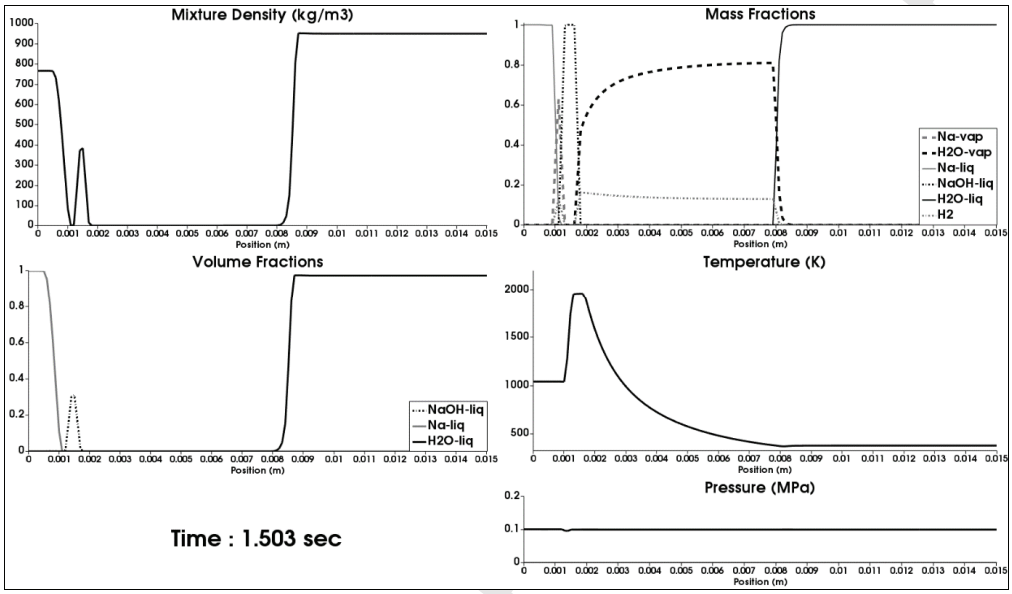

Figure 5.8: 1D computed results related to the 1D SWR test problem of Figure 5.1 in the presence of fluid motion, heat diffusion, phase transition of water and sodium species, mass diffusion $(\text{with } \chi = 0.2 \text{ and } a = 0)$ and both surface and gas reactions (both considered instantaneous). The mesh made of 150 cells is still considered. Results are shown at time t=1.503s. At this stage, the gas film thickness has considerably increased. The liquid sodium temperature exceeds 1000K. The liquid soda film separates both sodium and water vapors present in large proportions.

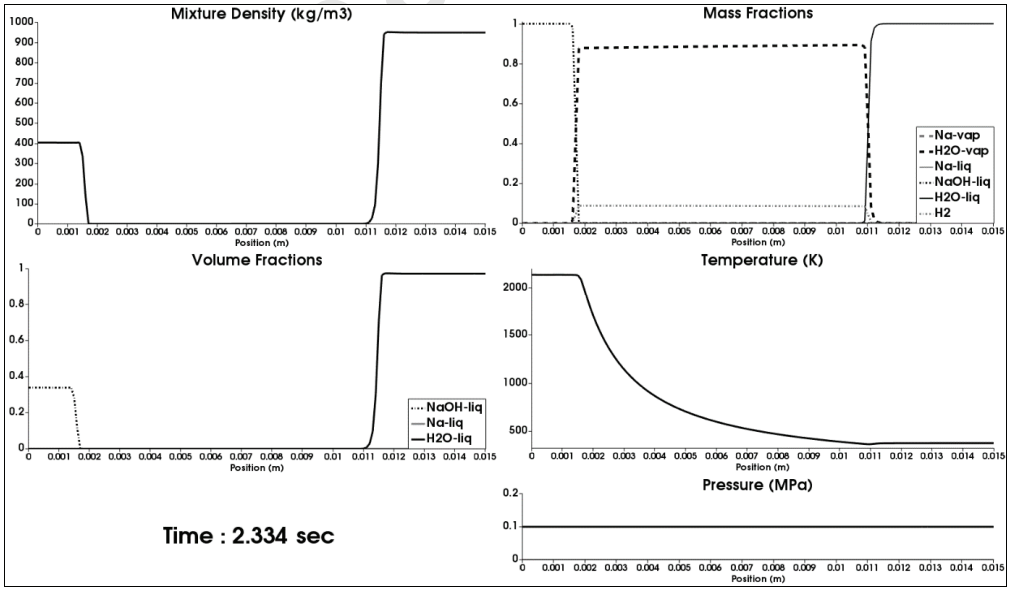

Figure 5.9: 1D computed results related to the 1D SWR test problem of Figure 5.1 in the presence of fluid motion, heat diffusion, phase transition of water and sodium species, mass diffusion $(\text{with } \chi = 0.2 \text{ and } a = 0)$ and both surface and gas reactions (both considered instantaneous). The mesh made of 150 cells is considered again. Results are shown at time

t=2.334s. At this stage, the sodium has been fully consumed. A hot (about 2000K) soda drop is formed at the place occupied initially by sodium.

At time 2.334s (Figure 5.9), liquid sodium has exceeded boiling point ($\approx 1156K$ at atmospheric pressure) and sodium vapor has been fully consumed. It results in hot $(\approx 2000K)$ liquid soda drop formation. The gas film continues to grow, while the soda drop gradually cools. No explosion (with shock wave emission) is observed. The pressure is nearly uniform in the Figures 5.2 to 5.9.

Three main points emerge of the former 1D numerical experiments:

- The diffuse interface model is able to model at least qualitatively the complex physics present in SWR process;
- The combustion regime observed in these tests is governed by thermal and mass diffusion. As the distance increases monotonically versus time the various gradients and associated fluxes decrease forbidding explosion occurrence;
- A liquid soda layer appears close to the sodium surface, lowering gas mass diffusion from the liquid water surface.

These observations motivate multi-D modelling, as illustrated in Figure 5.10. Indeed, the gas layer width is selected as a result of the various diffusive and reactive effects, in competition with gas ejection at the free surface and weight of the sodium drop. Multi-D effects are expected to maintain intense gradients oppositely to 1D computations.

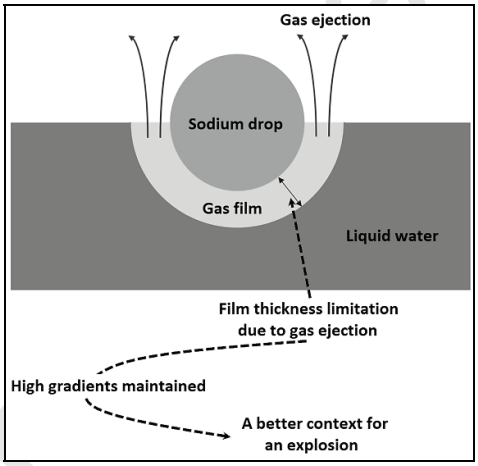

Figure 5.10: Schematic representation of the motivations for 2D computations. The gas layer width is selected by the competition of heat and mass diffusion, phase transition, exothermicity of the various reactions against gas ejection and weight of the sodium drop.

6. 2D computation of the sodium/water flow with reactions

The various physical effects considered in System (2.1) are now considered to compute various 2D configurations typical of sodium/water flow configurations with surface and gas phase chemical reactions. Two 2D tests are considered.

'Cold' liquid sodium drop (T=500K) in hot liquid water (T=370K)

The initial configuration is shown in Figure 6.1. In the present computations, the gas phase reaction is assumed instantaneous. Furthermore, turbulent diffusion is not considered at this stage (a=0) as well as phase transition of soda.

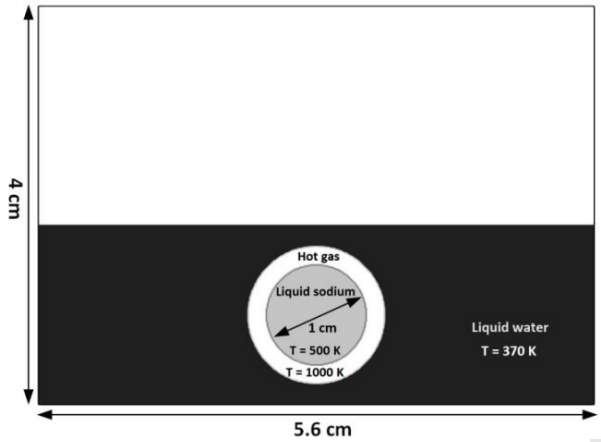

Figure 6.1: A liquid sodium drop is immersed in hot liquid water. Initially a hot gas made of nitrogen (T=1000K) separates both liquids. Nitrogen is also above liquid water surface (T=300K). The entire domain is closed, and the pressure is initially atmospheric.

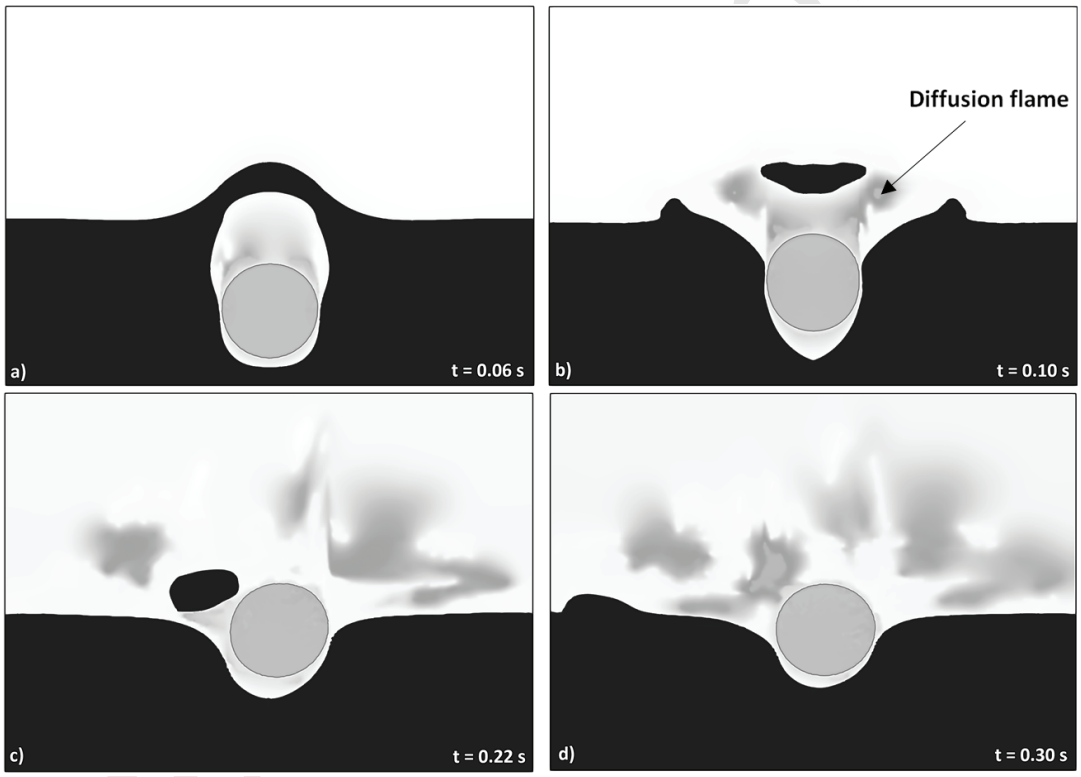

Figure 6.2: 2D computed results related to the test problem of Figure 6.1 in the presence of fluid motion, heat diffusion, phase transition of water and sodium species, mass diffusion (without turbulent amplification: a=0), both surface and gas reactions, gravity and capillary effects. The gas reaction is supposed instantaneous. The 2D mesh is made of 224 000 square cells. Results are shown at several times. The liquid water is shown in black through its volume fraction, whereas the liquid sodium drop is shown in grey. Elevated temperature zones are shown in shades of grey around the drop, showing the diffusion flame presence and burnt gases. Thermochemical Leidenfrost-type effect is reproduced.

Computed results are shown in Figure 6.2. Several stages appear during time evolution.

a) During the first time instants, the immersed liquid sodium drop reacts with water vapor, through a diffusion flame. Pressure and temperature increase setting to motion the various liquid-gas interfaces and increasing the gas pocket volume.
b) The hot gas pocket reaches the liquid water surface and breaks the liquid film. Surface waves propagate to the left and right of the liquid-gas interface while a liquid water fragment is

projected vertically. The sodium drop moves up and the diffusion flame between sodium and water vapors increases intensity.

c) The sodium drop is now in quasi-steady equilibrium and floats on the liquid water surface, still separated by the gas layer, whose thickness has been selected by the various diffusive effects, exothermicity of the reaction, weight of the sodium drop and gas flow in the interstice. The drop continues its autonomous motion as reported in the experiments.

The Leidenfrost-type effect, due to thermochemical transformations is thus at least qualitatively reproduced with the flow model and numerical method developed in the former sections. In the authors knowledge this is the first time such autonomous motion is reproduced numerically.

Some comments on the observed asymmetry can be made. The liquid water cap is ejected as a Rayleigh-Taylor type instability and falls with the same type of instability. Computing such instability in the presence of surface tension is challenging. When computing instabilities, symmetry can be lost for many reasons. In the present frame, surface tension effects add significant complexity. As shown for example in Figure 4.7, curvature is not constant around the circle, even with the regularization steps of Renardy and Renardy (2002). Moreover, in the experiments and in computations, the drop has spin motion, disrupting symmetry.

According to SWR experiments made at CEA Cadarache (Daudin, 2015), explosions seem to appear when sodium vaporization becomes significant. The boiling temperature at atmospheric pressure is about 1156K while in the present computations, the liquid sodium temperature is about 530 K at the end of the computations, corresponding to a significant temperature rise of 30K in 0.3s. However, with the present mesh very long computational time is needed to reach sodium boiling temperature. Therefore, computations have been carried out with lower mesh density and sodium boiling point has been reached. However, no explosion has been observed. It should be noted that when the mesh is coarsened, roughness appears at the sodium interface, without consequences on the physics but with results of bad visual quality.

As shock waves are emitted in the experiments, modelling improvements have to be addressed. Although numerical experiments have shown that consideration of soda presence and phase transition was not responsible for shock wave appearance, phase transition of soda is activated in the following for sake of completeness.

Furthermore, effects of chemical kinetics in the gas phase is reconsidered. In the former computations gas phase reaction was considered instantaneous resulting in diffusion flames and not premixed ones. As diffusion flames are inappropriate for pressure wave emission, premixing is now considered and needs delayed ignition through finite rate chemistry (option (b) of Section 2.5). Presence of turbulent diffusion roughly modelled through coefficient ‘a’ in Relation 2.7 is then expected to enhance water and sodium vapors mixing prior to gas reaction runaway.

A 2D axisymmetric configuration is considered in the following test. The initial configuration is schematized in Figure 6.3. The various physical effects considered in System (2.1) are activated. Finite rate chemistry and turbulent diffusion are considered in the gas phase for this run, as well as soda phase transition. The numerical results are shown in Figure 6.4. Six stages appear during time evolution.

a) During the first instants, the immersed liquid sodium drop reacts with the water vapor through the surface reaction. Pressure and temperature increase setting to motion the various liquid-gas interfaces and increasing gas pocket volume.

b) The hot gas pocket reaches the liquid water surface and induces liquid film breakup. Surface waves propagate to the left and right of the liquid-gas interface while a liquid water fragment is projected vertically. The sodium drop moves up and its temperature $T^L_{N_a}$ continues to increase as a consequence of surface reaction combined to heat diffusion ($T^L_{N_a} = 735K$).

c) When the liquid water fragment falls, thickness of the gas film separating the two liquids decreases significantly and surface reaction intensifies. A large amount of sodium vapor locally appears and mixes with the water vapor. When the liquid water fragment is very close

to the sodium drop, the temperature of the thin gas layer separating both liquids sharply increases and reaches the threshold temperature (1250 K) of gas phase reactions. The premixed reactive vapors strongly react and a shock is emitted. It also leads significant deformation of the sodium drop, fragmentation and vertical ejection of a small sodium drop. The drop is ejected at velocity about 1.7 m/s.

d) Later, the residual sodium drop reaches the water surface and floats, still separated from the liquid water by a gas layer. Same thermochemical Leidenfrost type effect as in Figure 6.2 happens. At time t=0.81s, sodium temperature reaches 879 K.

e) At time t=1.06s ($T_{N_a}^{L} = 910K$), a new shock wave is emitted and the explosion projects the sodium drop outside the domain, at velocity about 0.5m/s. This explosion results of vapors premixing inside the gas film under sodium drop, that has reached ignition temperature of gas phase reactions.

f) After sodium drop ejection, the water surface returns to its equilibrium state under the effect of gravity.

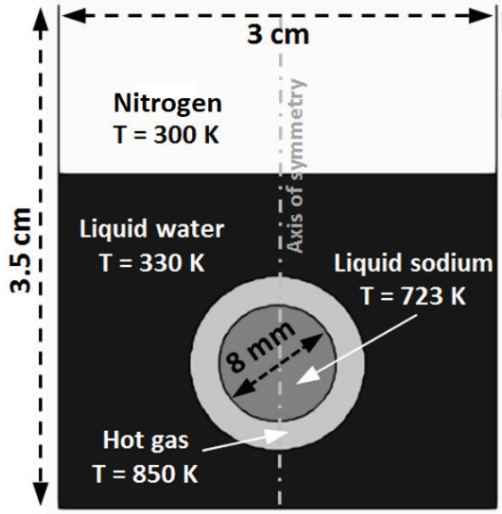

Figure 6.3: A 4mm radius liquid sodium drop is initially immersed in liquid water. Initially a hot gas made of hydrogen separates both liquids. Nitrogen is above the liquid water surface. The pressure is initially atmospheric in the whole domain. The top of the domain is treated as an outflow/inflow boundary condition as detailed in Appendix B, the tank being made of nitrogen at atmospheric conditions. The geometrical configuration being 2D axisymmetric, the computational domain is the half of the one represented.

It therefore appears that explosion can be qualitatively reproduced by the present model and is a consequence of gas premixing and delayed ignition through finite rate chemistry.

Pressure signals have been computed underwater and, in the atmosphere, closed to the interface. Pressure spikes of about 0.2 bar within liquid water and about 5000 Pa within the atmosphere have been recorded, in agreement with reported experimental data available at CEA Cadarache.

Furthermore, maximum computed temperature reached in the domain has been recorded versus time. Flame temperatures between 1600 and 1800 K have been detected, in very close agreement with the one measured (1670K) in SOCRATE experiments (Carnevali, 2012).

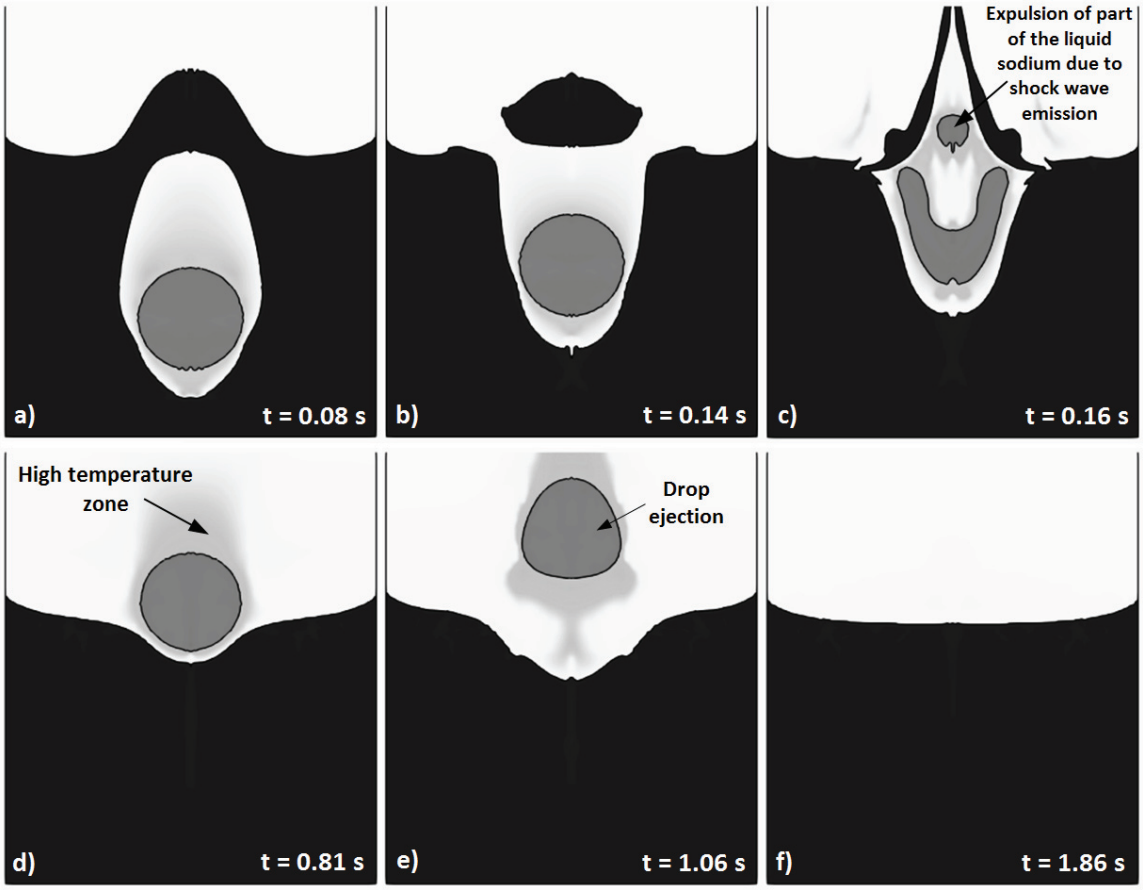

Figure 6.4: 2D axisymmetric computed results in the presence of compressible fluid motion, heat diffusion, phase transition of sodium, water and soda, mass diffusion in the gas phase, surface reaction, gas reaction with delayed ignition, gravity and capillary effects. Turbulent mixing of sodium and water vapors has also been considered in the gas film (a=3000). The geometric configuration being 2D axisymmetric, the calculation domain is the half of the one represented. The associated mesh is made of 25 725 square cells. Results are shown at several times. The liquid water is shown in black through its volume fraction, whereas the liquid sodium drop appears in dark grey. Elevated temperature zones are shown in shades of grey around the drop.

7. Conclusion

A diffuse interface model in temperature and pressure equilibrium has been used to compute contact and reaction between sodium and liquid water through a gas film. Many physical and chemical effects have been considered such as:

- sodium surface reaction,
- gas phase reaction,
- surface tension and buoyancy,
- phases compressibility,
- phase transition at interfaces,
- heat and mass diffusion,
- soda production and related phase transition,
- turbulent mixing in the gas layer.

Thanks to this modelling, two main effects have been qualitatively reproduced:

- The thermo-chemical Leidenfrost-type effect responsible for autonomous drop motion, as shown in Figure 6.2, in agreement with experimental observations;
- Explosion effect with shock wave emission and sodium ejection (Figure 6.4).

It seems that the present work provides the first qualitative reproduction of these events with a numerical approach.

From the present computations, it seems that explosion is a result of turbulent mixing of the various vapors, resulting in a premixed flame and not a diffusion one, as speculated before.
Many perspectives emerge to improve present qualitative observations:

- Determination of the chemical kinetics of sodium vapor with water vapor;
- Use fine enough resolution to capture subscale physics such as bubbles dynamics in the vicinity of the gas film, responsible of turbulent mixing;
- Improve knowledge of mass diffusion coefficients.

A key point relies in the numerical treatment of surface tension effects. Two regularizations have been used in the present study, with the color function and curvature computation. Efforts must be done to improve related computations. Another numerical issue is related to the consideration of mass diffusion in the context of diffuse interface formulations. The difficulty has been outlined in Section 5 with a possible cure but needs extra efforts to become general.

Acknowledgement
The authors are grateful to Alexandre Chiapolino, François Fraysse and Alexandre Allou for their help and expertise along the project.

References

Aksenova, A., Chudanov, V., Leonov, A. and Makarevich, A. (2017) Direct numerical simulation of two-phase gas dynamic flows with phase transition for water and for liquid sodium. MATEC Web of Conferences 115, 05009

Brackbill, J. U., Kothe, D. B., & Zemach, C. (1992) A continuum method for modeling surface tension. *Journal of computational physics*, *100*(2), 335-354

Carnevali, S. (2012) Unsteady aspects of sodium-water reaction: water cleaning of sodium containing equipments. *PhD thesis, CEA-UTC*

Carnevali, S., Proust, C. and Soucille, M. (2013) Unsteady aspects of sodium-water-air-reaction. *Chemical Engineering Research and Design, 91(4),* 633-639

Chase, M. W., Jr. (1998) NIST-JANAF Thermochemical Tables, Fourth Edition, *J. Phys. Chem. Ref. Data, Monograph 9*, 1-1951

Chiapolino, A., Boivin, P. and Saurel, R. (2017a) A simple and fast phase transition relaxation solver for compressible multicomponent two-phase flows. *Computers & Fluids, 150*, 31–45

Chiapolino, A., Saurel, R. and Nkonga, B. (2017b) Sharpening diffuse interfaces with compressible fluids on unstructured meshes. *Journal of Computational Physics, 340*, 389–417

Chudanov, V. V., Aksenova, A. E., & Leonov, A. A. (2019) Method of Solving Problems of Two-Phase Heat- and Hydrodynamics with Sodium Coolant. Atomic Energy, 1-7

Daubert, T. E., Danner, R. P., Sibul, H. M. and Stebbins, C. C. (1994) Physical and Thermodynamic Properties of Pure Compounds: Data Compilation. *Taylor & Francis, Bristol, PA.*

Daudin, K. (2015) Contribution à la prédiction des effets des réactions sodium-eau: application aux pertes de confinement dans un bâtiment générateur de vapeur d'un réacteur à neutrons rapides refroidi au sodium. *PhD thesis, CEA-UTC*

Daudin, K., Beauchamp, F., and Proust, C. (2018) Phenomenological study of the pre-mixing step of sodium-water explosive interaction. *Experimental Thermal and Fluid Science, 91, 1-8*

David, L., Beauchamp, F., Allou, A., Saurel, R., Guiffard, P. and Daudin, K. (2019) A small scale experiment and a simplified model to investigate the runaway of sodium-water reaction. Int. J. of Heat and Mass Transfer, submitted

Davis, S. F. (1988). Simplified second-order Godunov-type methods. SIAM Journal on Scientific and Statistical Computing, 9(3), 445-473

Deguchi, Y., Takata, T., Yamaguchi, A., Kikuchi, S. and Ohshima, H. (2014) Experimental and numerical reaction analysis on sodium-water chemical reaction field. Mechanical *Engineering Journal, 2(1), DOI: 10.1299/mej.14-00029*

Fink, J. K. and Leibowitz, L. (1995) Thermodynamic and Transport Properties of Sodium Liquid and Vapor. *Reactor Engineering Division, Argonne National Laboratory*

Gallice, G. (2002) Solveurs simples positifs et entropiques pour les systèmes hyperboliques avec terme source. Comptes Rendus Mathématique, 334(8), 713-716.

Garrick, D. P., Owkes, M. and Regele, J. D. (2017) A finite-volume HLLC-based scheme for compressible interfacial flows with surface tension. *Journal of Computational Physics,* 339, 46-67

Giovangigli, V. (2012) Multicomponent flow modeling. *Science China Mathematics, 55(2),* 285-308

Gosse, L. (2000) A well-balanced flux-vector splitting scheme designed for hyperbolic systems of conservation laws with source terms. Computers & Mathematics with Applications, 39(9-10), 135-159

Grove, J. W. (2010) Pressure-velocity equilibrium hydrodynamic models. *Acta Mathematica Scientia*, *30*(2), 563-594

Kapila, A. K., Menikoff, R., Bdzil, J. B., Son, S. F., & Stewart, D. S. (2001) Two-phase modeling of deflagration-to-detonation transition in granular materials: Reduced equations. *Physics of* fluids, 13(10), 3002-3024

Kee, R. J., Rupley, F. M., & Miller, J. A. (1989) Chemkin-II: A Fortran chemical kinetics package for the analysis of gas-phase chemical kinetics (No. SAND-89-8009). Sandia National Labs., Livermore, CA (USA).

Le Martelot, S., Saurel, R. and Nkonga, B. (2014) Towards the direct numerical simulation of nucleate boiling flows. *International Journal of Multiphase Flow, 66,* 62-78

Le Metayer, O., Massoni, J. and Saurel, R. (2013) Dynamic relaxation processes in compressible multiphase flows, Application to evaporation phenomena. *ESAIM Proceedings, 40*, 103–123

Le Metayer, O. and Saurel, R. (2016) The Noble-Abel Stiffened-Gas equation of state. *Physics of Fluids, 28(4),* 046102

LeVeque, R. J. (1998) Balancing source terms and flux gradients in high-resolution Godunov methods: the quasi-steady wave-propagation algorithm. Journal of computational physics, 146(1), 346-365

Lide, D., R. (2009) CRC Handbook of Chemistry and Physics, *CRC Press, 90th ed, 2804 p.*

Lund, H. (2012) A hierarchy of relaxation models for two-phase flow. *SIAM Journal on Applied Mathematics*, *72*(6), 1713-1741

Marfaing, O. (2014) Contributions to the fine-scale modeling of sodium-water reaction. *PhD thesis*, *UMPC, CEA*

Marfaing, O., Beccantini, A., Gounand, S., Monavon, A. and Studer, E. (2014) Semi-analytical and numerical investigation of a reactive gaseous film between two evaporating liquids. *International Journal of Heat and Mass Transfer, 71*, 562-572

Perigaud, G., & Saurel, R. (2005) A compressible flow model with capillary effects. *Journal of Computational Physics*, *209*(1), 139-178

Renardy, Y. and Renardy, M. (2002) PROST: A Parabolic Reconstruction of Surface Tension for the Volume-of-Fluid Method. *Journal of Computational Physics*, 183, 400-421

Roe, P. (1985) Some contributions to the modelling of discontinuous flows. Large-scale computations in fluid mechanics, 163-193

Saurel, R., Boivin, P. and Le Metayer, O. (2016) A general formulation for cavitating, boiling and evaporating flows. Computers & Fluids, 128, 53-64

Saurel, R. and Pantano, C. (2018) Diffuse-interface capturing methods for compressible two-phase flows. *Annual Review of Fluid Mechanics, 50*, 105-130

Saurel, R., Petitpas, F. and Abgrall, R. (2008) Modelling phase transition in metastable liquids: application to cavitating and flashing flows. *Journal of Fluid Mechanics, 607*, 313-350

Schmidmayer, K., Petitpas, F., Daniel, E., Favrie, N., & Gavrilyuk, S. (2017) A model and numerical method for compressible flows with capillary effects. Journal of Computational Physics, 334, 468-496

Takata, T., and Yamaguchi, A. (2003) Numerical Approach to the Safety Evaluation of Sodium–Water Reaction, Journal of Nuclear Science and Technology, 40(10), 708–718

Takata, T., Yamaguchi, A., Uchibori, A. and Ohshima, H. (2009) Computational Methodology of Sodium-Water Reaction Phenomenon in Steam Generator of Sodium-Cooled Fast Reactor. *Journal of Nuclear Science and Technology, 46:6,* 613-623*, DOI: 10.1080/18811248.2007.9711568*

Toro, E. F., Spruce, M. and Speares, W. (1994) Restoration of the contact surface in the HLL-Riemann solver. *Shock Waves, 4,* 25–34

Toro, E. F. (2013). Riemann solvers and numerical methods for fluid dynamics: a practical introduction. Springer Science & Business Media

Uchibori, A., Watanabe, A., & Ohshima, H. (2012) Numerical analysis of supersonic gas jets into liquid pools with or without chemical reaction using the SERAPHIM program. Nuclear Engineering and Design, 249, 35-40

Van Leer, B. (1979). Towards the ultimate conservative difference scheme. V. A second-order sequel to Godunov's method. Journal of computational Physics, 32(1), 101-136

Wood, A., B. (1930) A textbook of sound. *Bell Eds*

Zhang, X. and Shu, C.W. (2011) Positivity-preserving high order discontinuous Galerkin schemes for compressible Euler equations with source terms, *Journal of Computational Physics*, 230, 1238-1248

Appendix A. Mass diffusion – Compatibility with the second law of thermodynamics

Let us consider the simplified situation of a two-phase mixture made of liquid "L" and two-component gas "g", in 1D configuration. Mass diffusion only occurs within the gas mixture. Each phase (liquid and two-species gas) is assumed to occupy its own volume, and the gas mixture obeys Dalton's law.

To clarify the analysis, the model is written as follows, as a simplification of (2.1) in the absence of gravity, capillary effects, phase change, heat diffusion and chemical reactions:

$$\begin{aligned}
&\frac{\partial \alpha_g \rho_g y_1}{\partial t} + \frac{\partial \alpha_g \rho_g y_1 u + \alpha_g F_1}{\partial x} = 0 \\
&\frac{\partial \alpha_g \rho_g y_2}{\partial t} + \frac{\partial \alpha_g \rho_g y_2 u + \alpha_g F_2}{\partial x} = 0 \\
&\frac{\partial \alpha_L \rho_L}{\partial t} + \frac{\partial \alpha_L \rho_L u}{\partial x} = 0 \\
&\frac{\partial \rho u}{\partial t} + \frac{\partial \rho u^2 + p}{\partial x} = 0 \\
&\frac{\partial \rho E}{\partial t} + \frac{\partial u(\rho E + p) + \alpha_g Q}{\partial x} = 0
\end{aligned} \qquad \text{(A.1)}$$

y_1 and y_2 represent the mass concentrations within the gas phase ($y_1 + y_2 = 1$).

Mass concentrations of the phases may be used as well,

$Y_g = \frac{\alpha_g \rho_g}{\rho}$ and $Y_L = \frac{\alpha_L \rho_L}{\rho}$.

Terms F_1 and F_2 represent mass diffusion terms and $Q = \sum_k h_k F_k = (h_1 - h_2) F_1$ represents the associated energy flux. Expressions for F_1 and F_2 have to be determined. Obviously, $F_1 + F_2 = 0$.

The total energy is defined by,

$$E = Y_1 e_1 + Y_2 e_2 + Y_L e_L + \frac{1}{2} u^2,$$

with $Y_1 = y_1 Y_G$ et $Y_2 = y_2 Y_G$.

System (A.1) is expressed with Lagrangian derivatives:

$$\frac{dy_1}{dt} = -\frac{1}{\alpha_g \rho_g} \frac{\partial \alpha_g F_1}{\partial x}\ ;\ \frac{dy_2}{dt} = -\frac{1}{\alpha_g \rho_g} \frac{\partial \alpha_g F_2}{\partial x}\ ;\ \frac{dY_g}{dt} = 0\ ;\ \frac{dY_L}{dt} = 0\ ;\ \frac{d\rho}{dt} = -\rho \frac{\partial u}{\partial x}\ ;$$

$$\frac{du}{dt} = -\frac{1}{\rho} \frac{\partial p}{\partial x} \text{ and } \frac{de}{dt} + p \frac{dv}{dt} + \frac{1}{\rho} \frac{\partial \alpha_g Q}{\partial x} = 0 \qquad \text{(A.2)}$$

To obtain the entropy equation of the two-phase mixture the gas mixture one has to be determined first. It is based on the Gibbs identity of a given gas species,

$$T \frac{ds_k}{dt} = \frac{de_k}{dt} + p_k \frac{dv_k}{dt}.$$

Note that the partial pressure appears in this definition. In the specific context of ideal gas mixtures, specific volumes v_k are defined as:

$$y_k v_k = v_g.$$

From the Gibbs identity of each gas component the gas mixture Gibbs identity is obtained as,

$$T \frac{d(y_1 s_1 + y_2 s_2)}{dt} = \frac{d(y_1 e_1 + y_2 e_2)}{dt} + p_1 \frac{dy_1 v_1}{dt} + p_2 \frac{dy_2 v_2}{dt} + (g_2 - g_1) \frac{dy_1}{dt}$$

with,

$$g_k = e_k + p_k v_k - T s_k.$$

We thus have,

$$T \frac{ds_g}{dt} = \frac{de_g}{dt} + p \frac{dv_g}{dt} + (g_2 - g_1) \frac{dy_1}{dt} \qquad \text{(A.3)}$$

For the liquid phase, the Gibbs identity reads:

$$T\frac{ds_L}{dt}=\frac{de_L}{dt}+p\frac{dv_L}{dt} \tag{A.4}$$

with $v_L=\frac{1}{\rho_L}$.

Note that in (A.3) and (A.4) the pressure p is present instead of the partial one.

The two-phase mixture Gibbs identity is thus obtained as,

$$T\frac{ds}{dt}=\frac{de}{dt}+p\frac{dv}{dt}+(g_2-g_1)\frac{dY_g y_1}{dt},$$

where the mixture entropy is defined as $s=Y_L s_L+Y_g s_g$.

This result is reported in the energy equation (A.2):

$$T\frac{ds}{dt}+(g_1-g_2)\frac{dY_g y_1}{dt}+\frac{1}{\rho}\frac{\partial\alpha_g Q}{\partial x}=0$$

After some manipulations, we have:

$$\frac{\partial\rho s}{\partial t}+\frac{\partial\rho su+(s_1-s_2)\alpha_g F_1}{\partial x}=-\frac{\alpha_g F_1}{T}(v_1\frac{\partial p_1}{\partial x}-v_2\frac{\partial p_2}{\partial x})$$

With the mass diffusion fluxes defined by (2.2) non-negative entropy production is guaranteed:

$$\frac{\partial\rho s}{\partial t}+\frac{\partial\rho su+(s_1-s_2)\alpha_g F_1}{\partial x}=\frac{\alpha_g F_1^2}{T}\frac{p}{C}(v_1+v_2)>0$$

Appendix B. Inflow/outflow boundary condition

Tank boundary condition, with imposed pressure, temperature and mass fractions, is considered in this appendix. Under certain circumstances the inflow may become an outflow and reversely. Mathematical analysis of the mechanical and thermal equilibrium model considered in the paper shows the propagation of 3 waves at speeds: u, $u-c$ and $u+c$. For the sake of simplicity, we assume that the tank is located to the left of the first internal domain computational cell. Figure B.1 shows wave emission at the boundary between the tank and the first computational cell.

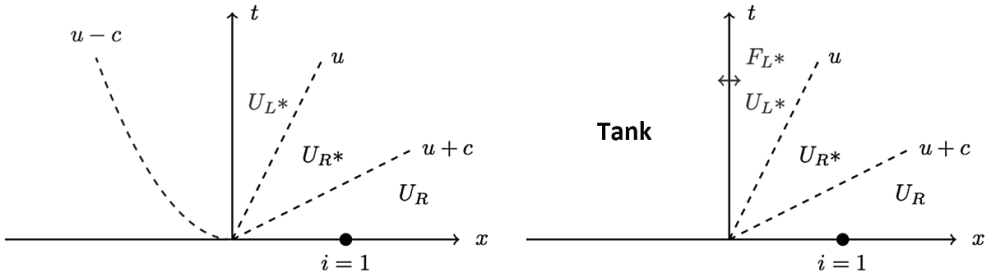

Figure B.1: Schematic representation of wave emission in the (x,t) diagram for a tank inlet boundary condition

The tank being infinitely large, wave propagating in the tank at the speed $u-c$ becomes curved as a result of 3D effects. However, in multi-dimension, jump relations are unknown for such wave. Assuming quasi-steady flow between the tank state, denoted by '0' and the inlet, stagnation enthalpy and entropy invariance provide appropriate relations. However, for the present flow model the equations of state being sophisticated, isentropic transformations are approximated from the sound speed definition,

$$c_L^{2^*}=c_0^{\,2}\approx\frac{p^*-p_0}{\rho_L^*-\rho_0},$$

where c denotes the mixture sound speed.

It provides mixture density at the inlet,

$\rho_L^* = \rho_0 + \frac{p^* - p_0}{c_0^2}$.

In addition, the total enthalpy is conserved between the tank and the inlet section. Thus:

$H_0 = H_L^* = e_0 + \frac{p_0}{\rho_0} = e_L^* + \frac{p^*}{\rho_L^*} + \frac{1}{2}u^{*2}$.

Combining these two relations a function of the pressure p^* is obtained:

$$e_L^*(p^*) - e_0 + \frac{p^* c_0^2}{\rho_0 c_0^2 + (p^* - p_0)} - \frac{p_0}{\rho_0} + \frac{1}{2}u^{*2}(p^*) = 0 \quad \text{(B.1)}$$

The mixture internal energy is defined as follows:

$e = \sum_{k=1}^{N} Y_k e_k(\rho, p)$

Using the NASG equation of state governing each phase, it is possible to re-express this definition as follows:

$$e = \bar{q} + (v(p) - \bar{b})B(p), \quad \text{(B.2)}$$

with $\bar{q} = \sum_{k=1}^{N} Y_k q_k$, $\bar{b} = \sum_{k=1}^{N} Y_k b_k$ and $B(p) = \frac{\sum_{k=1}^{N} Y_k c_{v,k} \frac{p + \gamma_k p_{\infty,k}}{p + p_{\infty,k}}}{\sum_{k=1}^{N} Y_k c_{v,k} \frac{\gamma_k - 1}{p + p_{\infty,k}}}$.

In addition, equation (B.1) requires the knowledge of $u^{*2}(p^*)$ which is determined by considering Rankine-Hugoniot jump relations through the wave $u + c$ propagating to the right:

$v_R^*(p^*) = v_R + \frac{2}{p^* + p_R}\left(e_R - e_R^*(p^*)\right)$.

$u^*(p^*) = -\sqrt{\frac{p_R - p^*}{v_R^*(p^*) - v_R}}\left(v_R^*(p^*) - v_R\right) + u_R$.

Inserting the equation of state (B.2) into (B.1) a function depending on p^* only is obtained:

$f(p^*) = \bar{q}_L^* + (v_L^*(p^*) - \bar{b}_L^*)B(p^*) - e_0 + \frac{p^* c_0^2}{\rho_0 c_0^2 + (p^* - p_0)} - \frac{p_0}{\rho_0} + \frac{1}{2}u^{*2}(p^*) = 0$.

An iterative method is used for its resolution.

Under certain circumstances the inflow may become an outflow. The 'inflow' velocity $u^*(p^*)$ becomes negative. In this case the wave pattern to consider is the one of Figure B.2:

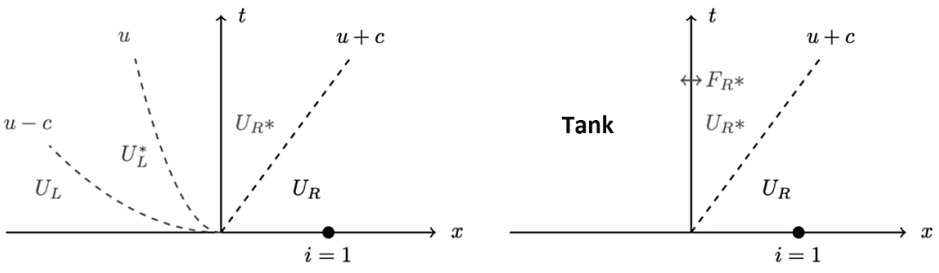

Figure B.2: Wave pattern when the inflow becomes an outflow. In that case the pressure p^* is prescribed to the tank pressure p_0.

The specific volume in the state R* is derived from the Hugoniot relation:

$v_R^*(p^*) = v_R + \frac{2}{p^* + p_R}\left(e_R - e_R^*(p^*)\right)$,

where $p^* = p_0$. The star velocity is computed with the same relation as before.

Declaration of interests

☒ The authors declare that they have no known competing financial interests or personal relationships that could have appeared to influence the work reported in this paper.

☐The authors declare the following financial interests/personal relationships which may be considered as potential competing interests: